

ARMY RESEARCH LABORATORY



**Enhancement of Army Operational Capabilities
With the Use of NPOESS Data**

**Sean G. O'Brien, Richard C. Shirkey,
and Barbara J. Sauter**

ARL-TR-2789

MARCH 2003

20030613 046

Approved for public release; distribution is unlimited.

NOTICES

Disclaimers

The findings in this report are not to be construed as an official Department of the Army position unless so designated by other authorized documents.

Citation of manufacturers' or trade names does not constitute an official endorsement or approval of the use thereof.

DESTRUCTION NOTICE—Destroy this report when it is no longer needed. Do not return it to the originator.

U.S. Army Research Laboratory
Technical Publications
Document Control, Bldg 1622
White Sands Missile Range, NM 88002-5501
Errata Sheet

Correction to: ARL report

Report number: ARL-TR-2789

Report title: Enhancement of Army Operational Capabilities Using NPOESS Data

Report authors: Sean G O'Brien, Richard C. Shirkey, Barbara J. Sauther

Problem	Replace
p 41 eq 16 printed over figure 48	p 41 with attached new p 41, 42

20030613046

A444750

Army Research Laboratory

White Sands Missile Range, NM 88002-5513

ARL-TR-2789

MARCH 2003

Enhancement of Army Operational Capabilities With the Use of NPOESS Data

Sean G. O'Brien
New Mexico State University

Richard C. Shirkey and Barbara J. Sauter
Computational and Information Sciences Directorate, ARL

Approved for public release; distribution is unlimited.

Preface

Coordination among U.S. infantry, armor, airborne, and special force elements has improved as new command, control, communications, computers, and intelligence technologies have matured and been fielded. Unfortunately, many of these technologies have also been made available to active and potential opponents of this nation. The end of the "Cold War" has seen the transfer of many advanced armaments and communication equipment to rogue states, terrorist groups, and endemic guerilla movements around the world. Those who are trained in the effective operation of modern military equipment represent a credible threat to relatively small rapid deployment forces sent abroad by the United States or its allies. Frequently, adversaries enjoy the advantage of time and terrain in the preparation of defenses, ambushes, and counterattacks in the vicinity of their redoubts.

In such an environment, any resource that "leverages" the technological advantages of the U.S. Army and its sister services may spell the difference between rapid success or extended stalemate in tactical operations. One domain that has a driving role in Army operations is the weather that encompasses the battlefield. The commander in today's Army has substantial new environmental tools for enhanced situational awareness, which were unavailable until very recently. The U.S. Army Research Laboratory (ARL) has been instrumental in creating a number of these new tools. One example is the Integrated Meteorological System, a mobile system that integrates meteorological satellite data, weather forecast models, data visualization utilities, and tactical decision aid (TDA) applications for timely use by the war fighter.

New sources of weather and other environmental data will soon be available that markedly improve weather characterization over remote or data-denied areas. In this report, we examine the interaction of TDA model predictions with one such data source, the proposed National Polar-orbiting Operational Environmental Satellite System (NPOESS). NPOESS and similar weather satellite platforms follow polar orbits that are much closer to the earth than geo-synchronous satellites and thus have much higher spatial resolution. The current Department of Defense polar-orbiting system, the Defense Meteorological Satellite Program (DMSP), has considerably lower spatial resolution than does the nominal NPOESS system, and the DMSP lacks the calibrated radiance imaging necessary to retrieve atmospheric optical depths that is available from NPOESS. We investigated the impacts that these NPOESS advantages have on target detection range estimates for low altitude sensors viewing tank or bunker-type targets.

Contents

List of Figures	iv
List of Tables	vi
Executive Summary	1
1. Introduction	5
2. Comparison of Parameter Resolutions for the DMSP and NPOESS Platforms	6
3. Input Parameter Selection for TAWS/NOWS Sensor Impacts	8
3.1 Clutter	8
3.2 Battlefield-Induced Contaminants (BIC)	9
3.3 Cloud Amount	11
3.4 Surface Visibility	12
4. Impact Study Design and Results	12
4.1 Design	12
4.2 Results	14
5. Individual Parameter Uncertainty Effects	20
5.1 Precipitation	20
5.2 Surface Visibility or Atmospheric Optical Depth	22
5.3 Cloud Base Height and Cloud Cover	26
6. Data Latency Issues	31
7. Reconnaissance and Combat Asset Effects	35
7.1 Search Asset Effects	35
7.2 Combat Attrition Effects	42
8. Summary and Conclusions	44
9. References	48
10. Acronyms	49
Report Documentation Page	51

List of Figures

Figure 1.	Very large BIC region that is easily detected at both sensor resolutions	10
Figure 2.	Small BIC region that is detected by the higher resolution imager and is missed by the lower resolution sensor	11
Figure 3.	Larger BIC region that is centered at a pixel boundary; lower resolution sensor still fails to detect the event	11
Figure 4.	Larger BIC region that is centered on a DMSP pixel center; DMSP detects the BIC event in this instance	11
Figure 5.	Main effects for NOWS 50% probability of detection range	15
Figure 6.	Two-factor parameter interaction effects for NOWS detection range	15
Figure 7.	TAWS main effects for 50% probability of detection range: Dense and sparse vegetation backgrounds	16
Figure 8.	Two-factor interaction effects for TAWS detection range: Dense and sparse vegetation backgrounds	16
Figure 9.	TAWS main effects for 50% probability of detection range: Snow and sparse vegetation backgrounds	17
Figure 10.	TAWS two-parameter interaction effects for detection range: Snow and sparse vegetation backgrounds	17
Figure 11.	Original fractal density distribution, resolution 0.01 km, threshold level 0.0, area above threshold 14.82 km ²	18
Figure 12.	Simulated DMSP image, resolution 0.5 km, threshold level 0.0, area above threshold 15.00 km ²	18
Figure 13.	Simulated NPOESS image, resolution 0.1 km, threshold level 0.0, area above threshold 15.30 km ²	18
Figure 14.	Original fractal density distribution, threshold level 0.5, area above threshold 3.16 km ²	19
Figure 15.	Simulated DMSP image, threshold level 0.5, area above threshold 5.25 km ²	19
Figure 16.	Simulated NPOESS image, threshold level 0.5, area above threshold 4.01 km ²	19
Figure 17.	Fifty percent threshold map for original resolution, with average detection ranges shown (in km)	19
Figure 18.	Same as previous figure but for DMSP	19
Figure 19.	Same as previous figure but for NPOESS	19
Figure 20.	Overlay of DMSP 50% detection range perimeter over original resolution map	20
Figure 21.	Overlay of NPOESS 50% detection range perimeter over original resolution map	20
Figure 22.	TAWS detection range spread for 5-mm/hr steady precipitation	21
Figure 23.	TAWS detection range spread for 10-mm/hr steady precipitation	22
Figure 24.	TAWS detection range spread for 20-mm/hr steady precipitation	22
Figure 25.	Geometry for computation of surface fractional cloud cover from 2-D cloud mask	27
Figure 26.	Sample fractal cloud distribution, 50-km by 50-km grid	28
Figure 27.	1000-ft cloud base fractional cloud cover, 0.1-km resolution	29
Figure 28.	1000-ft fractional cloud cover, 0.4-km resolution	29
Figure 29.	1000-ft fractional cloud cover, 0.55-km resolution	29

Figure 30. 1000-ft fractional cloud cover, 2.7-km resolution	29
Figure 31. 5000-ft cloud base fractional cloud cover, 0.1-km resolution	30
Figure 32. 5000-ft fractional cloud cover, 0.4-km resolution	30
Figure 33. 5000-ft fractional cloud cover, 2.7-km resolution	30
Figure 34. 10,000-ft cloud base fractional cloud cover, 0.1-km resolution	30
Figure 35. 10,000-ft fractional cloud cover, 0.4-km resolution	30
Figure 36. 10,000-ft fractional cloud cover, 2.7-km resolution	30
Figure 37. Detection range versus time for the "dry" (no precipitation), "actual" (short precipitation event), and "wet" (extended precipitation event) scenarios	33
Figure 38. Short period data latency effects for 6-hour rain event beginning at 0600 local time	33
Figure 39. Comparison of medium (3-hour) and long (10-hour) data latency period effects on TAWS detection range estimates	34
Figure 40. Long period data latency effects on TAWS detection range estimates	34
Figure 41. Estimated number N of search platforms required to search a 100- by 100-km area in 4 hours, for a 5-mm/hr steady rain	37
Figure 42. Required number of search platforms for a 10-mm/hr rain rate	38
Figure 43. Required number of search platforms for a 20-mm/hr rain rate	38
Figure 44. Estimated search time for a 100- by 100-km area with six observing platforms at a 5-mm/hr rain rate	39
Figure 45. Comparison of DMSP and NPOESS refined estimated search time uncertainties for a 5-mm/hr rain rate	40
Figure 46. DMSP and NPOESS refined search time comparison for a 10-mm/hr rain rate	40
Figure 47. DMSP and NPOESS refined search time comparison for a 20-mm/hr rain rate	41
Figure 48. DMSP and NPOESS uncertainties in search platform requirements for search of a 100- by 100-km area in 4 hours, 5-mm/hr rain rate	41

Tables

Table 1. Environmental effects with significant (✓) and major (x) impacts on detection range	2
Table 2. Comparison of resolutions for selected DMSP and NPOESS data products	8
Table 3. Base scenario parameters	13
Table 4. NOWS two-level parameters	13
Table 5. TAWS two-level parameters: dense/sparse vegetation backgrounds	14
Table 6. TAWS two-level parameters: snow/sparse vegetation backgrounds	14
Table 7. Visibility uncertainties for different haze layer upper boundary heights Z_H , with the NPOESS threshold resolution for optical depth and temperature profile	24
Table 8. NOWS detection ranges and uncertainties for AN/PVS-7 (third generation), for different haze layer upper boundary heights Z_H at 0100 local time	25
Table 9. TAWS detection ranges and uncertainties for TV sensor 3003 (U.S. Air Force Research Laboratory, 2001) for different haze layer upper boundary heights Z_H at 1200 local time	25
Table 10. TAWS detection ranges and uncertainties for IR sensor 1011 (U.S. Air Force Research Laboratory, 2001) for different haze layer upper boundary heights Z_H at 0000 local time	26
Table 11. TAWS detection ranges and uncertainties for IR sensor 1011 (U.S. Air Force Research Laboratory, 2001) for different haze layer upper boundary heights Z_H at 1200 local time	26
Table 12. Sample comparison of TAWS detection range results for variations of cloud base height and cloud fraction, using the Table 3 base scenario	30
Table 13. Summary of significant parameter main effect and interaction impacts	44
Table 14. Comparison of approximate TAWS IR detection range errors attributable to DMSP and NPOESS measurement uncertainties	45

Executive Summary

This report examines satellite representations of environmental conditions that significantly affect night vision goggle (NVG) and infrared (IR) sensors typically carried on Army helicopters and aircraft flying at low speeds and very low altitudes. Our study uses simulated data (with resolutions appropriate to the Defense Meteorological Satellite Program (DMSP) and the proposed National Polar-orbiting Operational Environmental Satellite System (NPOESS) polar orbiters) as environmental input to the Target Acquisition Weapons Software (TAWS) tactical decision aid (TDA). As a recent addition, TAWS now includes the Night vision goggles Operations Weather Software (NOWS) TDA.

Relative effects that data products from the current DMSP and future NPOESS platforms have on TDA results are topics of the study. Remotely sensed environmental properties can strongly influence the target detection range predicted by a TDA model in tactical scenarios. The TDA target detection range is therefore the metric that we have used to compare the quality of DMSP and NPOESS results. The discussion divides into two sections, both concerning tactical Army scenarios. The core of our study addresses direct impacts that these different satellite platform resolutions have on TDA detection range. An additional study section details secondary consequences of satellite data quality: data latency impacts, target search considerations, and war game implementation.

Core Study: TDA Performance

Background clutter, background type, and illumination type provided the most significant impacts for the NVG sensor that was examined in our study. Less significant effects on detection range were found for boundary layer height (the thickness of the aerosol haze layer that is adjacent to the surface of the earth), cloud cover, and battlefield-induced contaminants (BIC), i.e., dust, airborne debris, and smoke.

Two background pairs were examined for impacts on the operation of an IR sensor with narrow field of view (NFOV) and wide field of view (WFOV) scanning modes. Primary impacts came from precipitation, cloud cover, and (for the NFOV mode) BIC for the background pair comprised of dense and sparsely growing vegetation. Minor effects were seen for clutter and background type. The second background pair featured fresh snow and sparse dormant vegetation. The primary impacts were similar to those for the dense/sparse vegetation background pair, with the addition of background type having a significant effect. Minor effects attributable to season (i.e., primarily temperature changes) and clutter were also observed.

The impact study results are summarized in Table 1. Note that the TV sensor type was only examined for the case of derived surface visibility. Because of the similar operating wavelength band, it was assumed that TV impacts were similar to those for NVG sensors.

Table 1. Environmental effects with significant (√) and major (x) impacts on detection range

Sensor Type	Battlefield Environment Parameter							
	Clutter	Background Type	Precipitation	BIC	BLH*	Illumination	Cloud Cover	Surface Visibility
TV	‡	‡		‡	‡	‡	‡	√
NVG	x	x		√	√	x	√	
IR	√	x	x	x†			x	√

*BLH = boundary layer height

†NFOV mode only

‡ Impact assumed to be similar to NVG

Significant individual environmental parameters were surveyed with the parameter impact study results used as guides. When possible, DMSP resolution results were compared with those from the NPOESS. In cases when an environmental parameter cannot be directly measured by the DMSP (e.g., atmospheric optical depth), the discussion involved NPOESS alone.

Precipitation rate comparisons showed that DMSP-derived detection range uncertainties are 2 to 4 times larger than NPOESS for the wide range of selected precipitation rates. The results also demonstrate that the detection range uncertainty diminishes with increasing rain rate.

Surface visibility has significant effects on certain sensor types such as TV sensors. NPOESS can provide surface visibility data, but the DMSP platform cannot. This study found that the NPOESS-derived low altitude NVG detection range showed little effect for typical haze layer visibilities and boundary layer heights. The TV sensor showed the largest detection range response to haze layer visibility variation but relatively little response to boundary layer height variations. The IR sensor showed only moderate variations in detection range.

Cloud cover/base height differences between cloud cover patterns derived from the DMSP smooth resolution imagery and the NPOESS threshold resolution are largest for low clouds (with cloud bases below 1 kilometer (km) above ground level [AGL]). When cloud bases exceeded 2 km AGL, little difference for cloud cover results was seen between the DMSP fine and NPOESS threshold resolution results.

Overall, the NPOESS threshold resolution provides superior spatial and parametric characterization in comparison to that provided by the DMSP for several significant environmental parameters. From the Army standpoint, the most important of these are precipitation rate and cloud cover for NVG and IR sensors and to a lesser degree, meteorological visibility for visible band TV sensors. The calibrated radiometric data from the visible/infrared imager/radiometer suite sensor and the finer frequency coverage and spatial resolution of the microwave band conical microwave imager/sounder and cross-track infrared sounder sensors on NPOESS will make certain parameters (such as surface visibility, boundary layer height, and cloud base height) available at resolutions of practical use in Army TDA applications. The results presented herein demonstrate substantial improvements in data quality in comparison to

the data quality presently available from DMSP, even when the threshold NPOESS resolutions are considered.

Additional Study: Data Latency, Search Requirements, and War Gaming

As an additional study, we also examined the consequences of satellite parameter resolution on target detection range impacts because of data latency, asset allocations for target search, and war gaming input data requirements.

Data latency times that are significantly shorter than the duration of a sensor-impacting meteorological event cause peak detection range errors that can grow dramatically with the latency lag time. Under a light rain scenario that begins and ends abruptly, errors on the order of 10 km were noted, even for latency periods as short as 0.5 hour. More slowly varying meteorological events lead to smaller detection range errors in the TDA model predictions for a given data latency time; additional NPOESS satellite platforms would also mitigate latency impacts.

The time required to search a tactical area with a variable number of identical sensor platforms was examined with a simple model. The application of DMSP and NPOESS-resolution data and the TAWS model for a sample scenario indicated that estimated search times for a fixed number of sensor platforms or estimated number of platforms required for a fixed search time had markedly lower uncertainties when the NPOESS data were employed. It is anticipated that this finding will still be valid when more sophisticated search models are used.

Force-on-force attrition formulations used in war games vary according to the relative skill, operational doctrines, and equipment of the opposing forces. For most of these models, the individual values of the attrition rate coefficients or their ratio play a central part in the allocation of resources required to win or survive the engagement. The combined higher spatial and parametric resolution of NPOESS platform relative to DMSP leads to less uncertainty in the estimates of target acquisition times, more accurate estimates of attrition, and thus, increased confidence in derived simulation results. Since coupling the attrition rate coefficients required for the war-gaming simulations with TDA predictions for maximum target resolution would have required modifications of the underlying TDA source code, this task was left to subsequent studies.

INTENTIONALLY LEFT BLANK

1. Introduction

The Target Acquisition Weapons Software (TAWS) is a successor to the Air Force's Electro-Optical Tactical Decision Aid (EOTDA) (Touart et al., 1993) and with the advent of TAWS Version 3, includes the Night vision goggles Operations Weather Software (NOWS) (Gouveia, 1997). The EOTDA was a weather impacts decision aid disk operating system (DOS) program that simulated the performance of electro-optical sensors and various targets, primarily from an Air Force point of view, that is, with downward looking scenarios. TAWS, a graphical user interface (GUI)-based program running under the Windows operating system, is a tri-service program that includes additional Army and Navy sensor and target object models, provides revisions of the sensor performance model and other physics routines, accepts current or forecast weather data, and provides improved GUI input. Thus, TAWS accepts information concerning user-selected sensors and targets, combines this with automated or user input information about weather, and provides graphical or tabular output about the impacts that the weather has on the ability of the chosen sensor to acquire the selected target during the given weather conditions. The commander can then use this information for mission planning purposes or to ascertain which weapons platform can "see" the farthest in current or forecast weather conditions.

Because TAWS Version 3.0 was released after this study was started, TAWS Version 2.2 and NOWS Version 6.0 were used as surrogates. Other differences between TAWS Version 2.2 and TAWS Version 3.0, aside from the inclusion of NOWS, include a revised thermal performance model multi-service electro-optic signatures (MuSES) (Johnson et al., 1998) and replacement of the Schmieder sensor performance algorithm with the more widely accepted Night Vision and Electronic Sensor Directorate's (U.S. Army CECOM, 1995) Acquire model. For a detailed comparison of the differences between these two sensor performance algorithms, the reader is referred to Shirkey, Sauter, and Cormier (2001); for the purposes of this study, the results would remain the same.

To determine the maximum detection range to acquire a given target, a number of quantities need to be known: the target-to-background contrast, the atmospheric conditions, solar or lunar luminance, and sensor characteristics, all of which are spectrally variable. Many of these environmental entries to weather effects decision aids depend highly on detailed knowledge of the atmospheric state above a region of operational interest. Remote sensing technologies have improved to a point that many critical atmospheric state parameters may be obtained from sensors carried on board high altitude aircraft or satellite platforms.

It is important that the Army provides its viewpoint and emphasis in the application of TDA models such as TAWS or NOWS to its near-surface domain of activity. This is particularly true for the developing environmental data "feeds" from satellite sources, where sensor hardware and software improvements can significantly enhance TDA performance for data-denied areas

encountered in Army operations. Given this need and the opportunity to direct the future development of sensor suites available on board the next generation of satellite systems, it was deemed expedient to determine the performance improvement possible, given different choices and mixes of future sensors.

In this report, we discuss data provided by the Defense Meteorological Satellite Program (DMSP) and National Polar-Orbiting Operational Environmental Satellite System (NPOESS) polar orbiters, and specific illustrative scenarios. The intent here is to examine satellite representations of environmental conditions that significantly impact night vision goggle (NVG) and infrared (IR) sensors typically carried on Army helicopters and aircraft flying at low speeds and very low altitudes. We use earlier results from TDA sensitivity studies (e.g., Keegan, 1990, or Cormier, 2000) to define which environmental parameters should be considered in these assessments. Further, we will distinguish the impacts that data products from the older DMSP platforms have on the TDA performance relative to those from the future NPOESS platforms. Our principal metric for these comparisons is the 50% probability of detection range reported during variations from the base scenarios.

2. Comparison of Parameter Resolutions for the DMSP and NPOESS Platforms

The atmospheric sensor systems carried on board the DMSP series of polar orbiters include the Operational Line Scan system (OLS), Special Sensor Microwave Imager (SSM/I), Special Sensor Microwave Atmospheric Temperature Sounder (SSM/T-1), and the Special Sensor Microwave water vapor profiler (SSM/T-2).

The OLS has broadband visible-near IR (0.58 to 0.91 μm full width at half maximum [FWHM]) and far IR (10.3 to 12.9 μm FWHM) sensors, as well as a PMT (photo multiplier, 0.51 to 0.86 μm FWHM) sensor for low light operation. The OLS operates in two primary resolution modes. The higher resolution “fine” mode has a nadir spot size of 0.55 kilometer (km) that is used for special order data sets of regional interest. The low resolution “smooth” mode is an aggregation of fine mode data, which has a resolution of 2.7 km at nadir and is the primary operational mode for the OLS for global data sets. The PMT sensor also operates in smooth mode.

The SSM/I is a seven-channel, four-frequency (19 to 85 GHz) linearly polarized passive microwave sensor that provides data about precipitation over land and water, soil moisture, cloud liquid water, and land/sea surface temperatures (among other parameters). The longer operating wavelength for this instrument contributes to a much larger nadir spot size than that for the OLS—approximately 25 km diameter. The SSM/T-1 operates in seven channels in the 50- to 60-GHz band, providing vertical profiles of air temperature at a rather larger nadir spot size of 174 km diameter. Coarse vertical profiles and horizontal distribution of water vapor data are

provided by the SSM/T-2 sensor, which operates in three channels near a 183-GHz water vapor line (as well as in two window channels). The nadir spot size for this instrument is approximately 48 km in diameter.

Because the NPOESS sensor suite is being developed, performance specifications for sensor subsystems have been subject to periodic revision. These specifications are published in the NPOESS integrated operational requirements document (IORD). The IORD draft version 1A (Joint Agency Requirements Group, 2000) was used for some of the information in the following discussion. In this document (as in the case of the DMSP), two working horizontal spatial resolutions for the imaging sensors are anticipated: a lower resolution (called the “threshold” mode) and a higher resolution “objective” mode. Currently, the hardware development has only committed to the threshold resolution mode. The data products (environmental parameters) that are derived from the processing of raw sensor data are known as environmental data records (EDRs). Three of the NPOESS sensor suites will produce EDRs of interest from the TDA standpoint: the visible/infrared imager/radiometer suite (VIIRS), the conical microwave imager/sounder (CMIS), and the cross-track infrared sounder (CrIS).

VIIRS will operate in the visible to far IR spectral region (0.3 to 14 μm), providing information about clouds, atmospheric aerosols, and land/sea surface properties (from 26 EDRs). The principal advantage of VIIRS is that it combines the spectral resolution and radiometric accuracy of the Advanced Very High Resolution Radiometer (AVHRR) flown on National Oceanic and Atmospheric Administration’s (NOAA’s) polar orbiters with the horizontal spatial resolution of the DMSP OLS. The Moderate Resolution Imaging Spectro-radiometer (MODIS) that is carried on board the Terra (EOS AM-1) polar orbiter is similar to VIIRS in spatial and spectral resolution. The MODIS data should thus provide a surrogate for testing the processing and interpreting of VIIRS EDRs. The MODIS sensor (among others on Terra) also has “direct broadcast” capability, in which it can send data directly to an appropriately equipped earth station from space in near real time during an overpass. This ability may also prove convenient for testing data latency effects on TDA performance.

The NPOESS CMIS sensor package will perform functions analogous to the DMSP SSM/I sensor but with higher spectral and spatial resolution. This sensor system will provide information including temperature and moisture vertical profiles and their horizontal distribution, cloud properties, and sea surface winds (among data from 20 EDRs). Data for three EDRs will be supplied by CrIS, including temperature, moisture, and atmospheric pressure profiles. This sensor suite is similar to a combination of the DMSP SSM/T-1 and SSM/T-2 packages.

The data supplied from the IORD and other sources¹ allow us to compare the differences in parameter and spatial resolutions available from the DMSP and NPOESS platform sensor suites described previously. Table 2 summarizes such a comparison for a selected set of data products for these sensors at different operating resolutions; the selection is biased toward TDA

¹Private communication, McWilliams, 2001.

application and the discussion that follows. Those products that are unavailable or are of dubious availability are simply designated by "N/A" entries in the table.

Table 2. Comparison of resolutions for selected DMSP and NPOESS data products

Resolution Parameter/Spatial	DMSP (Smooth Mode)	DMSP (Fine Mode)	NPOESS (Threshold)	NPOESS (Objective)
Surface Visibility Horizontal	N/A	N/A	10 km	1 km
Cloud Amount: Horizontal	$\pm 10\%$ 25 km	$\pm 10\%$ 25 km	$\pm 10\%$ 25 km	$\pm 5\%$ 2 km
Cloud Base Height Horizontal	N/A N/A	N/A N/A	2 km 25 km	0.25 km 10 km
Clutter Horizontal	2.7 km	0.55 km	0.4 km	0.1 km
Rain Rate Horizontal	± 5 mm/hr 25 km	± 5 mm/hr 25 km	± 2 mm/hr 15 km	± 2 mm/hr 0.1 km
Boundary Layer Height Vertical	(N/A: Lowest channel peak is at 800 mb or about 2 km AGL)	(N/A: Lowest channel peak is at 800 mb or about 2 km AGL)	20 mb (about 0.17 km near the surface)	15 mb (about 0.12 km near the surface)
BIC Horizontal	2.7 km	0.55 km	0.4 km	0.1 km
Soil Moisture Horizontal	$\pm 10\%$ 25 km	$\pm 10\%$ 25 km	$\pm 10\%$ 4 km	$\pm 5\%$ 2 km

mb = millibars

In the table, we have displayed the low (smooth) and high (fine) spatial resolution modes for DMSP performance and the low (threshold) and high (objective) resolution mode performance for the NPOESS platform. The normal spatial resolution for DMSP data is the smooth mode for routine global coverage. When a specific region of interest is to be studied, the fine resolution mode is employed. The threshold NPOESS performance level is currently expected to be the routine operational mode for that system. Thus, when one considers the *normal* operational modes, it is apparent that the NPOESS platform has a distinct advantage over the DMSP in its spatial resolution.

3. Input Parameter Selection for TAWS/NOWS Sensor Impacts

3.1 Clutter

In general, the user-specified clutter level will have a substantial effect on target detection ranges in the TAWS/NOWS models. For small vehicular targets, the spatial resolution for clutter determination in a scene must be on the order of the size of the vehicle. Unfortunately, neither the DMSP (with its 0.6-km nominal maximum horizontal resolution) nor the 0.1-km objective mode resolution specification for the NPOESS visible/IR band will satisfy this requirement. On

the other hand, larger man-made targets such as buildings, bridges, rail yards, or dams do approach scales detectable by the DMSP/NPOESS sensor packages. The higher resolution NPOESS sensor is evidently better suited to the task of clutter estimation, although it is not entirely clear how surface clutter data obtained at small angles to the terrain surface normal (by satellite) will translate into estimates at larger angles characteristic of near-earth helicopter-borne sensors. It might also be argued that low spatial frequency clutter is a parameter that varies slowly with time and thus, could be better estimated from high-resolution data sets from satellite platforms such as the Landsat (land satellite system) or SPOT (*Satellite Pour l'Observation de la Terre*). This is probably true in many cases (particularly for arid regions), but the response of vegetation and other terrain elements to seasonal or episodic (i.e., storm induced) variations in precipitation argues for assessment of clutter on a shorter time scale. DMSP and NPOESS can provide such data on a daily basis.

For smaller targets (e.g., an individual tank in a column), the lower resolution satellite data may delineate zones of low clutter (such as patches of snow) from higher clutter areas (such as adjacent stands of trees or brush). Here, again, the higher resolution NPOESS imagery should provide more accurate input of this environmental parameter for target groupings measuring several hundred meters in extent.

The specification of clutter in the TAWS/NOWS models is essentially tri-state (low, medium, high). The effect of variation of this parameter for large targets should thus be investigated. It is expected that the lower resolution DMSP imagery will tend to bias estimates to the low end of the clutter scale.

3.2 Battlefield-Induced Contaminants (BIC)

The effect of BIC on TAWS/NOWS detection ranges is also pronounced, particularly when background haze levels are low. These contaminants normally are quite localized and quite inhomogeneous when they are present on the modern battlefield. Screening smokes have high extinction coefficient values in their applicable wavelength bands, so spatially small BIC events can have marked impacts on the sensor performance simulated by TAWS/NOWS. However, the treatment of BIC phenomena by TAWS/NOWS is rather crude, with a simple "present/not present" selector as the only parameter control available to the user. Thus, the implication is that the BIC event is present uniformly over the field of regard or line of sight (LOS) of a TAWS/NOWS scenario. While one might argue for a more sophisticated treatment of BIC in these models, the current situation requires that the satellite data be reduced to provide only a "yes/no" answer about the presence of BIC phenomena. In this case, the available resolution of the satellite data is critical.

To illustrate the role of DMSP versus NPOESS horizontal resolution, consider the following set of one-dimensional examples. Suppose that our criterion for signaling the presence of a BIC event is that the observed excess radiance of a pixel over the nominal background is 50% of the full-scale value that would be observed, for example, for a perfect reflector. The length of our

notional LOS is 6 km, and we have a Gaussian-distributed BIC event of the form $\exp(-(x-x_0)^2/\sigma^2)$, in which x is the distance from the origin on the LOS, x_0 is the distance of the center of the Gaussian BIC event from the LOS origin, and σ is the 1/e half-width of the Gaussian. The true form of the Gaussian function is plotted, along with the pixel width averages for resolutions of 0.6 km (DMSP fine mode) and 0.1 km (NPOESS objective mode). Figure 1 shows a result for a BIC event at the LOS midpoint ($x_0 = 3.0$ km) and with a rather large extent ($\sigma = 1.5$ km). Both sensor resolutions have multiple pixel registrations that are above the $L/L(\max) = 0.5$ threshold, easily detecting the event.

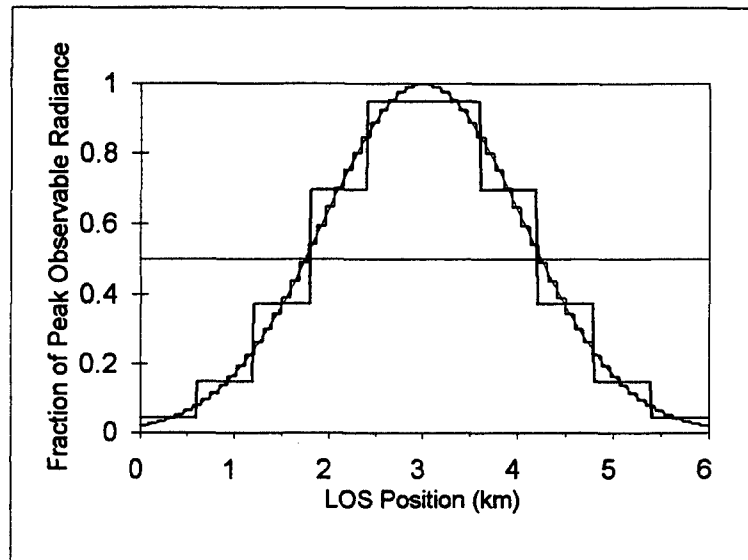


Figure 1. Very large BIC region that is easily detected at both sensor resolutions.

For a case when the BIC region is very small ($\sigma = 0.1$ km), Figure 2 illustrates that the higher resolution NPOESS imager detects the anomaly and that the DMSP fails to detect it by a wide margin. The same result holds for a slightly larger BIC region ($\sigma = 0.3$ km) in Figure 3, although the DMSP-resolution result comes much closer to detection at the 0.5 threshold. Figure 4 shows that a slight displacement of the BIC region center (from $x_0 = 3.0$ to $x_0 = 2.7$ km) creates a case when the lower resolution sensor does detect the BIC event. Thus, as one would expect, the detection of even large BIC events is a hit-or-miss affair for the lower resolution sensor when the events have sizes on the order of its resolution. In truth, neither sensor resolution is particularly adroit at spotting small but significant BIC concentrations that may be of interest in operations against smaller targets. Clouds much smaller than 100 m in extent will probably not be detected and used as model input.

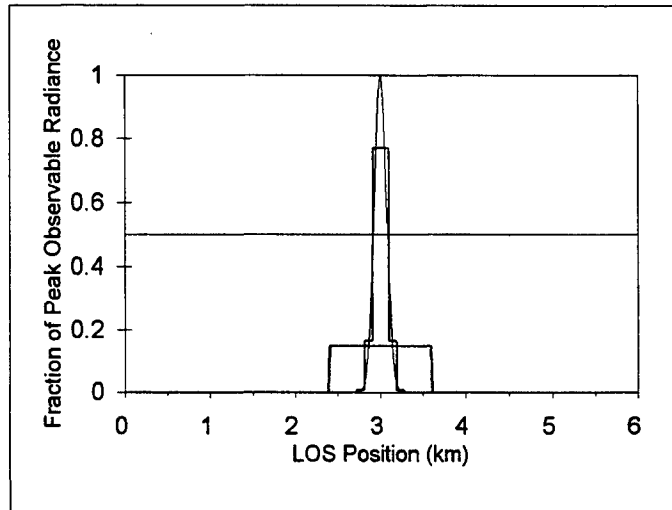


Figure 2. Small BIC region that is detected by the higher resolution imager and is missed by the lower resolution sensor.

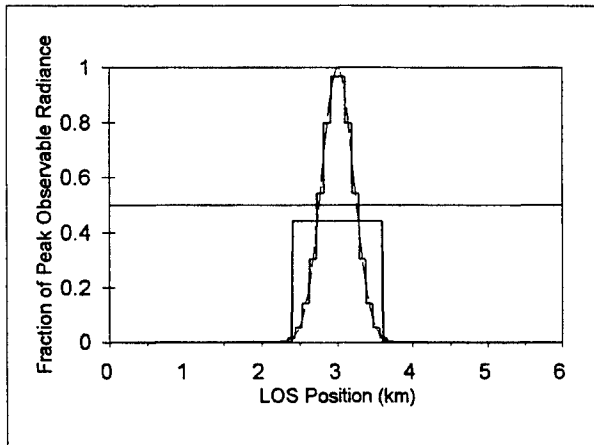


Figure 3. Larger BIC region that is centered at a pixel boundary; lower resolution sensor still fails to detect the event.

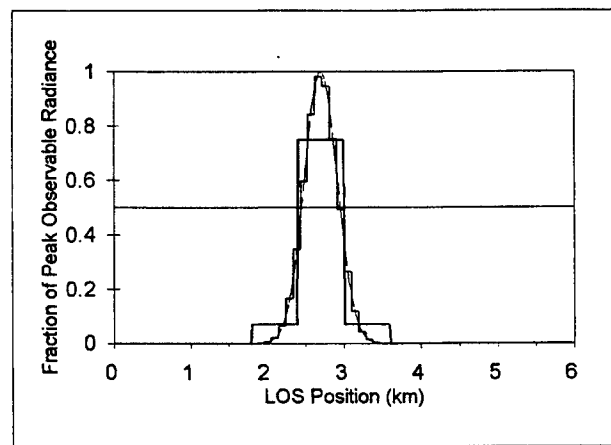


Figure 4. Larger BIC region that is centered on a DMSP pixel center; DMSP detects the BIC event in this instance.

3.3 Cloud Amount

Among the weather parameters in TAWS/NOWS that are given detailed treatment, cloud amount (or fractional cloud cover) is a particularly good example; this is no surprise, given the Air Force development heritage of TAWS/NOWS. Cloud cover is characterized by three input height ranges, each of which has a user-specifiable cloud type (including “none”), cloud base height, and cloud cover fraction (in eighths). When clouds are present for an Army near-surface mission, the cloud type does not strongly affect the NVG or IR detection range results, nor does the cloud base height (unless it intersects the sensor-target LOS). However, if low clouds are present, the cloud-free line of sight (CFLOS) estimate given by the TAWS/NOWS models is strongly affected by the cloud amount input. The cloud amount is, in turn, yielded by resolution-sensitive imagery. The remarks about detection of BIC “events” or clouds also apply here: the lower

resolution DMSP data will be less adept at detecting individual cloud puffs than will the higher resolution NPOESS sensor. Thus, one would expect that cloud amount estimates for partially cloudy conditions would be more accurate from the NPOESS sensor.

3.4 Surface Visibility

Results from earlier EOTDA sensitivity studies (e.g., Keegan, 1990) indicate that errors in estimates of surface visibility do not strongly affect visible or IR detection range results until low visibility conditions prevail. The horizontal spatial resolution of the DMSP/NPOESS sensors does play a role in the size of the visibility uncertainty, but this is primarily for cases when the distribution of boundary layer aerosol haze is not uniform and at least some sampled regions contain high aerosol levels. Such conditions would prevail during dust storms or blizzards, for example.

Because aerosol extinction varies slowly with wavelength and the wavelength dependence of the Rayleigh scattering is well defined, the spectral resolution of the EO sensor does not have to be very high in order to yield reasonably accurate estimates of the total atmospheric optical depth. However, the DMSP OLS sensor has such a large bandwidth response that it does not satisfy even this weak performance requirement. The NPOESS aerosol optical thickness requirement specified in the NPOESS IORD stipulates that the vertical optical depth of aerosols be obtained at multiple wavelengths within the 0.4- to 2.4- μm band. On-line documentation indicates that on the order of a dozen visible band channels and several IR channels will be used by the VIIRS system carried on board NPOESS. This should satisfy the wavelength resolution requirement outlined previously.

4. Impact Study Design and Results

4.1 Design

A study was designed to quantitatively assess the impact of principal sensed parameters upon TDA detection range performance, for the NOWS and TAWS base scenarios. The primary environmental parameters for each base scenario are shown in Table 3.

For this study, we have selected sensors from the user menus provided in NOWS (AN/PVS-7, third generation) and TAWS (U.S. Air Force Research Laboratory, 2001). The method used to assess the impact of variations away from the base scenarios employs a factorial design at two levels (Box, Hunter, & Hunter 1978). In this approach, a list of critical environmental parameters is developed for each TDA model. Each of these parameters is allowed to assume only two values (levels) at which the TDA is executed. The "main effect" $\Delta R_{\text{DET}}(\alpha)$ of each environmental parameter α is then simply the difference between the average (over all other parameters γ so that $\gamma \neq \alpha$) detection range calculated at one level of the parameter α_1 and the average at the other level α_0 :

$$\Delta R_{DET}(\alpha) = \bar{R}_{DET}(\alpha_1) - \bar{R}_{DET}(\alpha_0). \quad (1)$$

Table 3. Base scenario parameters

Parameter	NOWS	TAWS
Target	T-80 tank	T-80 tank
Background	Vegetation/Growing/Dense	Shrubs/Live/Dense
Sensor	AN/PVS-7, 3rd Gen.	IR
Illumination Condition	Full Moon	Sun
Surface Visibility	10 km	10 km
Wind Speed	0 knots	0 knots
Surface Temperature	12° C	7° to 17° C (diurnal variation)
Surface Dew Point	5° C	5° C
Cloud Amount	0/8 (clear)	0/8 (clear)
Surface Aerosol Type	Rural	Rural
Surface Albedo Type	Continental	Continental
Clutter Level	Low	Low
Boundary Layer Height	3000 feet	3000 feet
BIC	Not Present	Not Present
Tropospheric Layer	Default	Default

We may also define two-factor interactions between parameters α and β as one-half the difference of the main effect for one parameter (e.g., α) between states (β_1 and β_0) of the other:

$$\Delta R_{DET}(\alpha, \beta) = \frac{[\bar{R}_{DET}(\alpha_1, \beta_1) - \bar{R}_{DET}(\alpha_0, \beta_1)] - [\bar{R}_{DET}(\alpha_1, \beta_0) - \bar{R}_{DET}(\alpha_0, \beta_0)]}{2}. \quad (2)$$

The critical parameters used in the impact study are shown in Tables 4 through 6.

Table 4. NOWS two-level parameters

Parameter	Levels
Target Type	1 = T-80 tank 0 = Eglin AFB bunker
Illumination	1 = Full Moon 0 = New Moon
Clutter Level	1 = High 0 = Low
Background Type	1 = Shrubs/Growing/Dense 0 = Snow/Fresh/1 in Deep
Boundary Layer Height	1 = 100 ft. 0 = 3000 ft.
BIC	1 = Present 0 = Absent
Cloud Cover	1 = 8/8 (Overcast) 0 = 0/8 (Clear)

Table 5. TAWS two-level parameters: dense/sparse vegetation backgrounds

Parameter	Levels
Target Type	1 = T-80 tank (off state - 'cold') 0 = Eglin AFB bunker
Clutter Level	1 = High 0 = Low
Background Type	1 = Vegetation/Growing/Dense 0 = Vegetation/Dormant/Sparse
Soil Moisture	1 = Wet 0 = Dry
Seasonal Temperature Variation	1 = 7 - 17 C (Spring) 0 = 1 - 6 C (Winter)
Precipitation	1 = 5 mm/hr 0 = 0 mm/hr
BIC	1 = Present 0 = Absent
Cloud Cover	1 = 8/8 (Overcast) 0 = 0/8 (Clear)

Table 6. TAWS two-level parameters: snow/sparse vegetation backgrounds

Parameter	Levels
Target Type	1 = T-80 tank (off state - 'cold') 0 = Eglin AFB bunker
Clutter Level	1 = High 0 = Low
Background Type	1 = Snow/Fresh/1 inch depth 0 = Vegetation/Dormant/Sparse
Seasonal Temperature Variation	1 = 7 - 17 C (Spring) 0 = 1 - 6 C (Winter)
Precipitation	1 = 5 mm/hr 0 = 0 mm/hr
BIC	1 = Present 0 = Absent
Cloud Cover	1 = 8/8 (Overcast) 0 = 0/8 (Clear)

4.2 Results

The NOWS and TAWS TDAs were then exercised over the matrix of critical parameter variations. The resulting target detection ranges were then abstracted into spreadsheets, the main effects were calculated, and results were plotted at two observation times (0100 and 0345 for NOWS and 0000 and 1200 for TAWS). The results are shown in Figures 5 through 8.

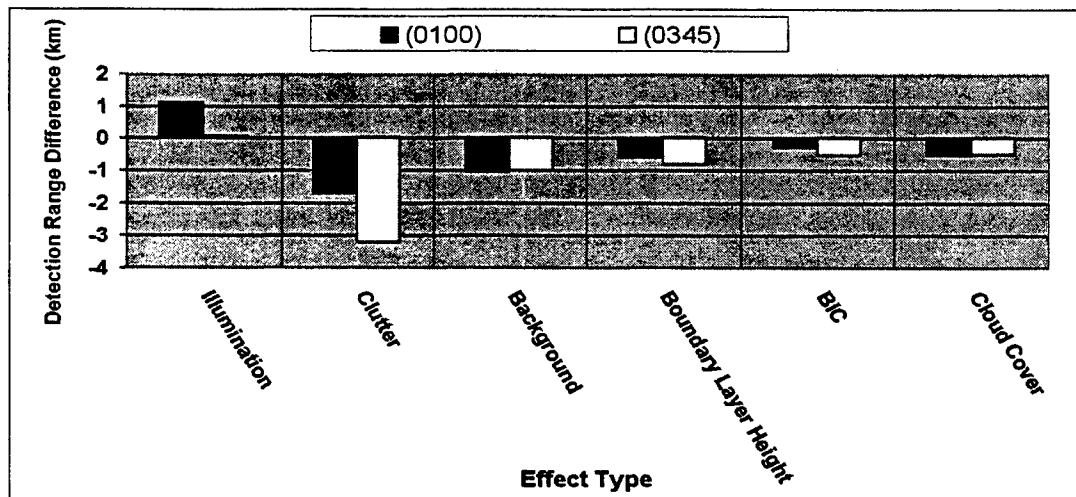


Figure 5. Main effects for NOWS 50% probability of detection range.

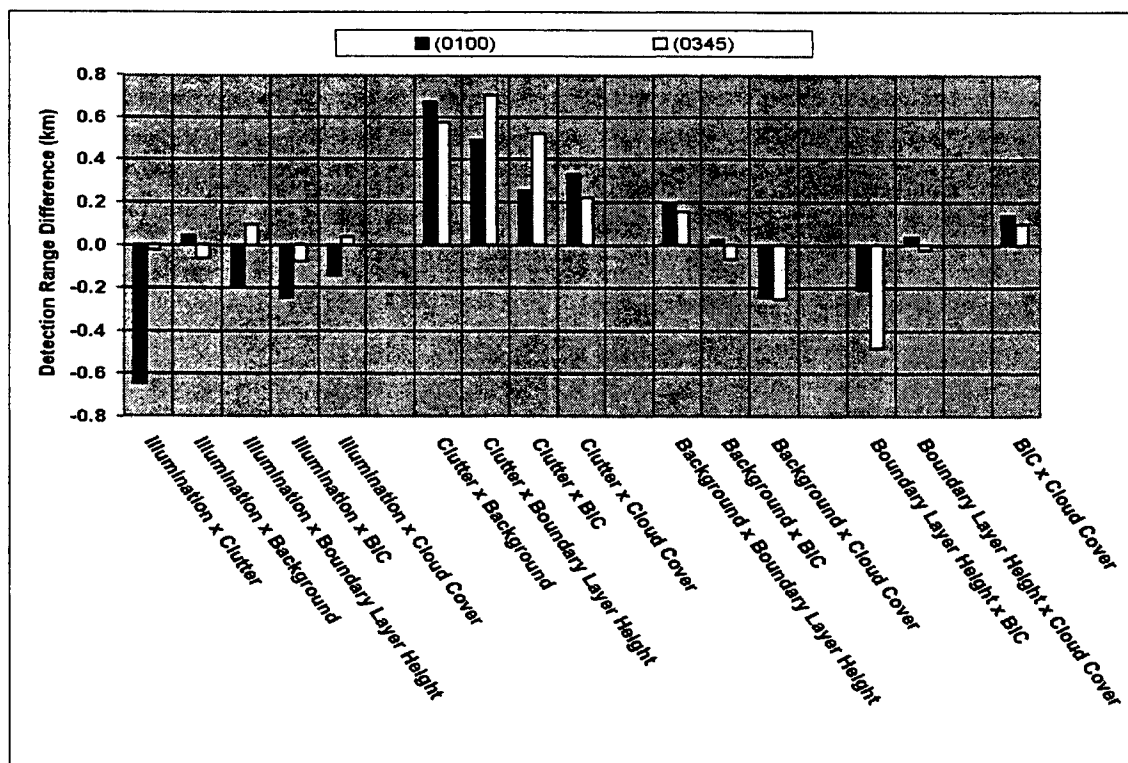


Figure 6. Two-factor parameter interaction effects for NOWS detection range.

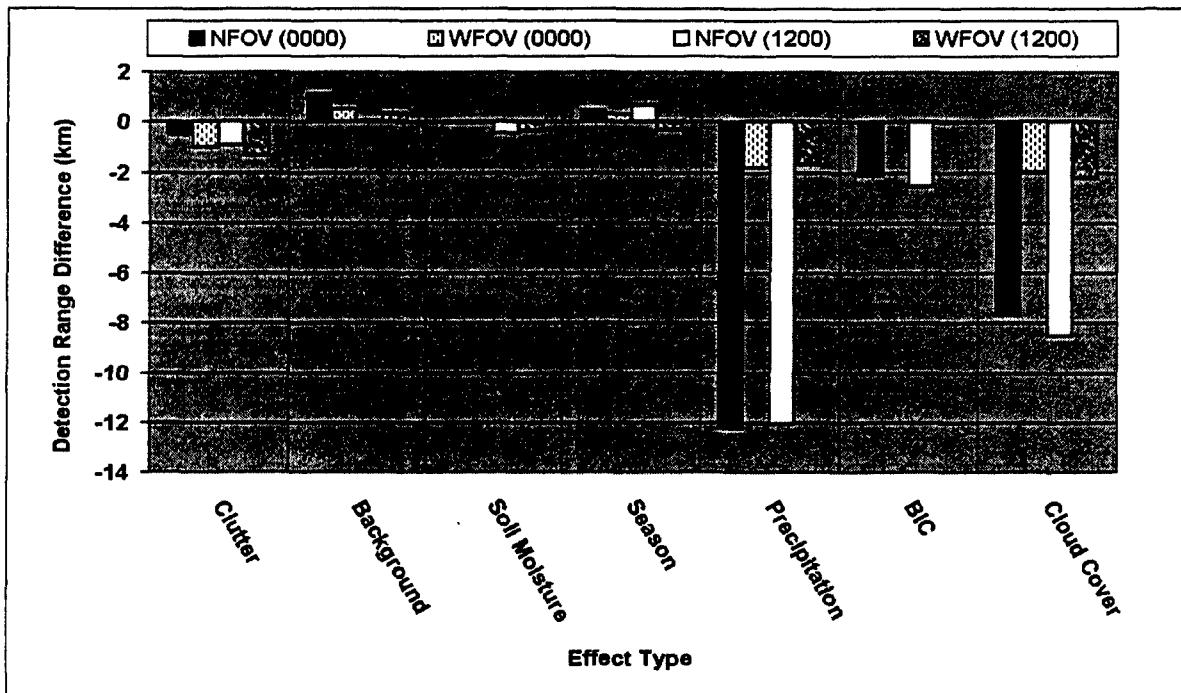


Figure 7. TAWS main effects for 50% probability of detection range: Dense and sparse vegetation backgrounds.

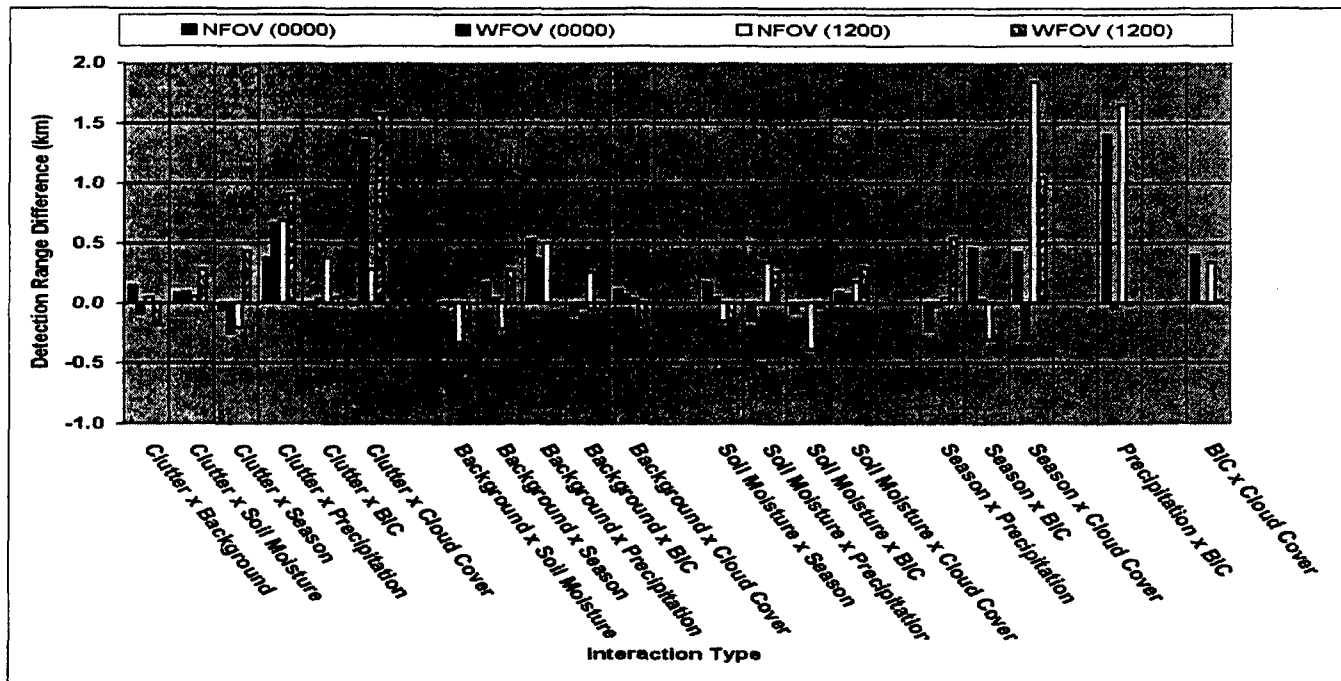


Figure 8. Two-factor interaction effects for TAWS detection range: Dense and sparse vegetation backgrounds.

Note that the main effects shown in the figures consist of the parameter “on” (level “1” in Tables 4 or 5) average minus the “off” (level 0) average. The results show that for NOWS, the primary environmental parameters that impact detection range are clutter and background type,

with some significant contributions from most of the secondary parameters. In the case of TAWS, precipitation, BIC and cloud cover strongly affect the detection range results (see Figures 9 and 10).

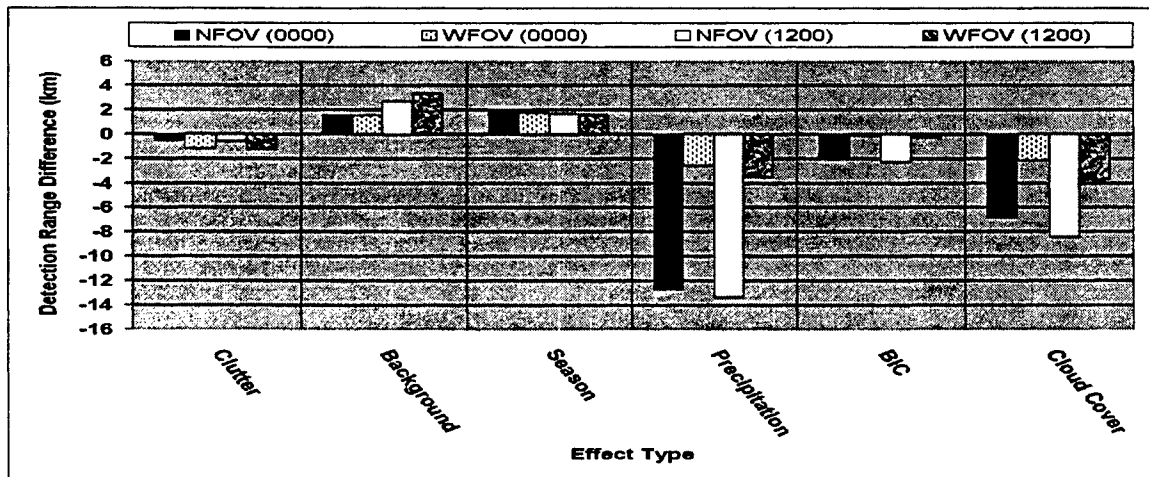


Figure 9. TAWS main effects for 50% probability of detection range: Snow and sparse vegetation backgrounds.

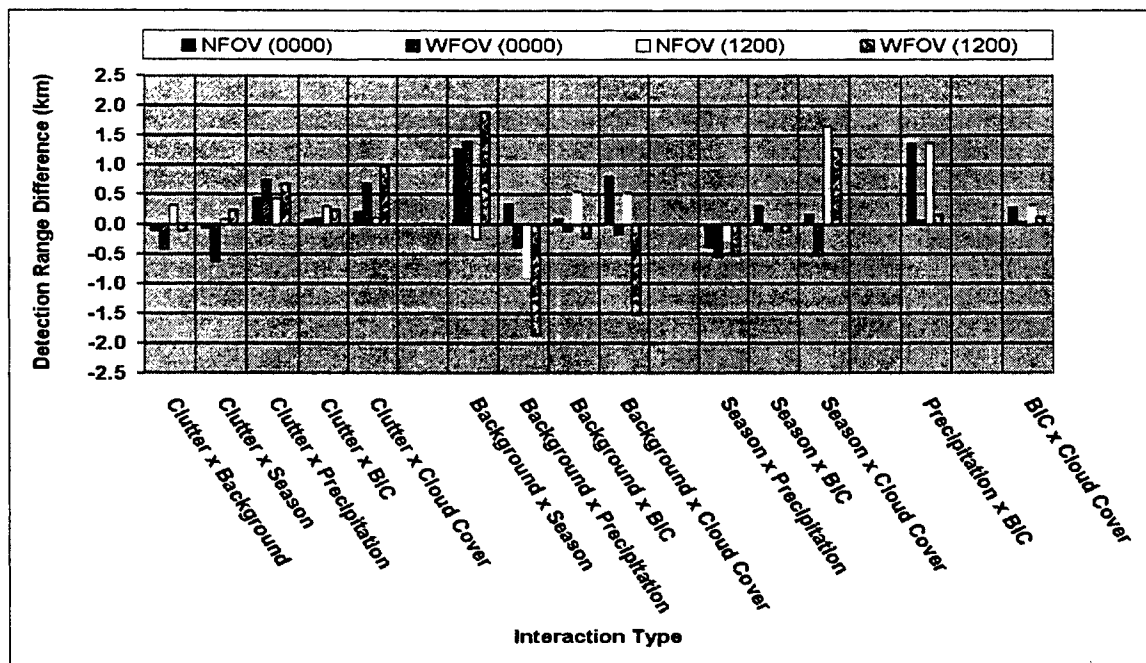


Figure 10. TAWS two-parameter interaction effects for detection range: Snow and sparse vegetation backgrounds.

The connection of these results to DMSP and NPOESS horizontal spatial resolution can be illustrated via a simple numerical example. Figures 11 to 13 show a fractal density distribution (Saupe, 1988) that might represent a cloud field (or another parameter distribution such as one of

precipitation or BIC) distributed over a 5-km by 5-km area. The original scene has a 10-m resolution and is displayed in Figure 11. Figure 12 displays how the low resolution DMSP sensor might record the scene at 0.5-km resolution. Figure 13 shows what the somewhat higher resolution (0.1 km) NPOESS visible/near-IR sensor might record. We generate the simulated DMSP and NPOESS images by summing the density values within the boundaries of each overlaid grid square (or "pixel") and then dividing by the pixel area.

The total scene area where the cloud density exceeds a zero threshold level is about 15 km² for all three resolution levels. However (as in Figures 14 to 16), when the threshold is set to 50% of the highest pixel value in each scene (which might, for example, be the arbitrary demarcation between zones of partial cloudiness and overcast conditions), the lower resolution (DMSP) results show a markedly larger (and somewhat differently shaped) area than either of the other resolutions. Since we know (from the impact study results) that the TAWS IR sensor is strongly affected by overcast conditions, the larger observed overcast area will indicate that the spuriously large low resolution zone will have lower detection ranges. This will impact "go/no-go" probability assessments derived from the combination of the TDA and satellite-derived environmental data. It will also impact real-time TDA-augmented assessments when satellite data are available in real time. Figures 17 through 19 illustrate how the TAWS ensemble average detection ranges would map into contiguous regions at the three resolutions. Figures 20 and 21 show that the NPOESS resolution data are significantly better than those for the DMSP, both in total area and perimeter conformity.

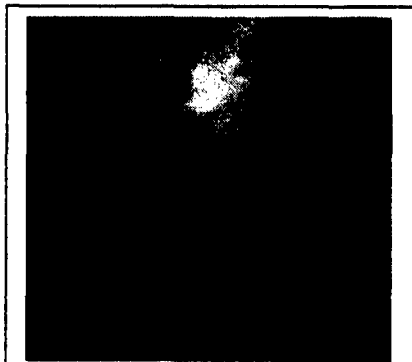


Figure 11. Original fractal density distribution, resolution 0.01 km, threshold level 0.0, area above threshold 14.82 km².

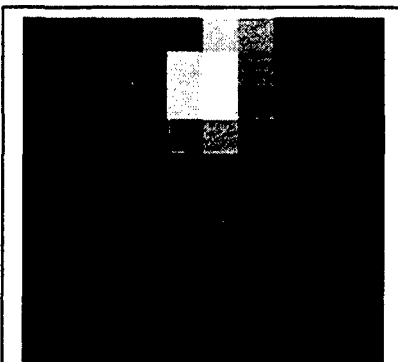


Figure 12. Simulated DMSP image, resolution 0.5 km, threshold level 0.0, area above threshold 15.00 km².

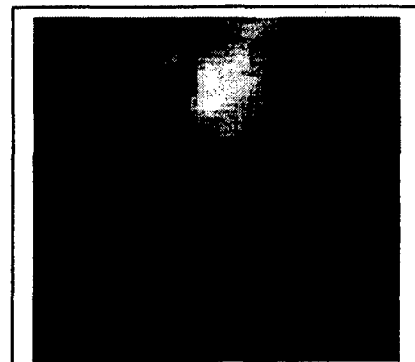


Figure 13. Simulated NPOESS image, resolution 0.1 km, threshold level 0.0, area above threshold 15.30 km².



Figure 14. Original fractal density distribution, threshold level 0.5, area above threshold 3.16 km².

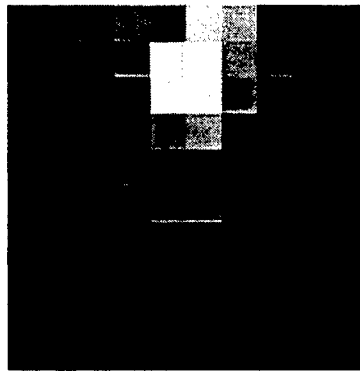


Figure 15. Simulated DMSP image, threshold level 0.5, area above threshold 5.25 km².

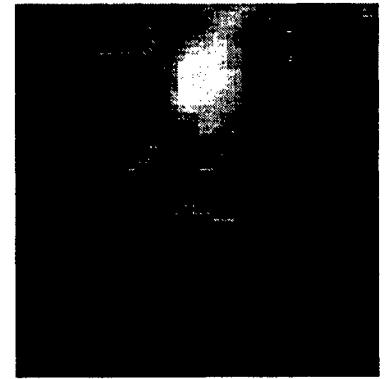


Figure 16. Simulated NPOESS image, threshold level 0.5, area above threshold 4.01 km².

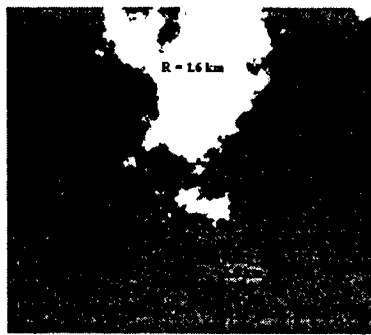


Figure 17. Fifty percent threshold map for original resolution, with average detection ranges shown (in km).

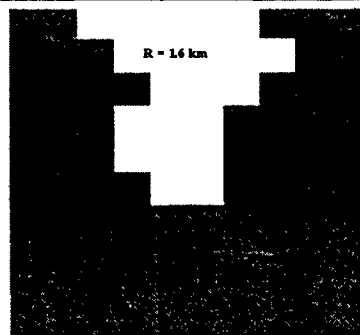


Figure 18. Same as previous figure but for DMSP.

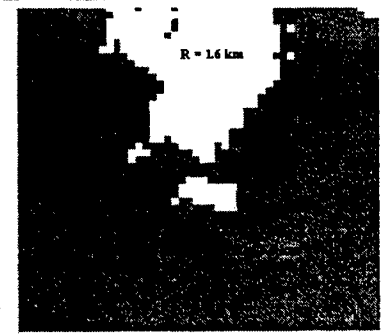


Figure 19. Same as previous figure but for NPOESS.

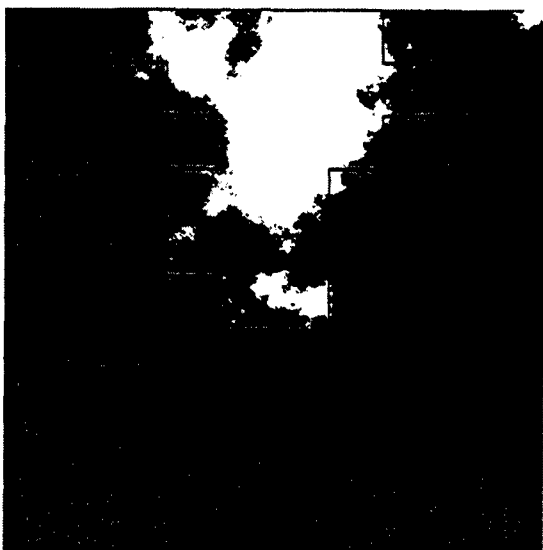


Figure 20. Overlay of DMSP 50% detection range perimeter over original resolution map.

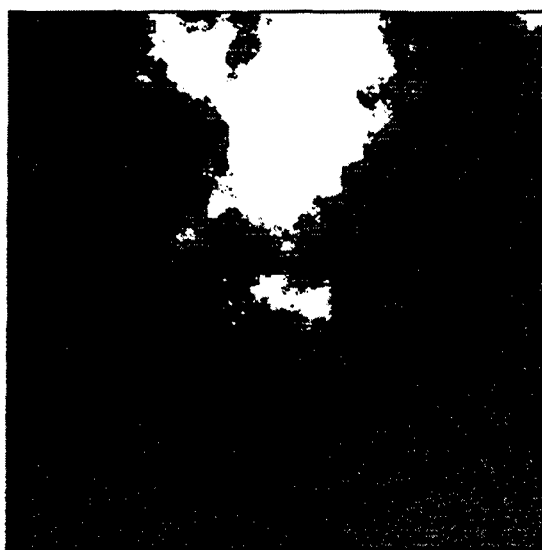


Figure 21. Overlay of NPOESS 50% detection range perimeter over original resolution map.

5. Individual Parameter Uncertainty Effects

In addition to the spatial resolution effects that satellite data products have on TAWS/NOWS model predictions, uncertainties in measured parameter values can have significant impacts on detection range results. The parameters that have the largest impacts for Army scenarios are examined next.

5.1 Precipitation

As indicated before, the uncertainty in the measurement of precipitation rates from the DMSP and NPOESS platforms will significantly affect the detection ranges predicted for IR sensors by the TAWS model. The DMSP nominal uncertainty in the precipitation rate (± 5 mm/hr) is roughly twice that projected for the NPOESS platform (2 mm/hr). The quantitative impact of this disparity on TAWS detection ranges may be appreciated with a slightly modified version of the TAWS base scenario from Table 2. Three parameters were modified from the original scenario: soil moisture was changed from dry to wet, a low overcast (8/8, low level) was substituted for the clear sky, and the precipitation (rain) rate was “stepped over” non-zero values (5, 10, and 20 mm/hr). The TAWS model was run for each extreme value in each platform’s envelope about the mean precipitation rate. The resulting detection ranges as functions of time were then plotted in Figures 22 through 24, with shading differentiating each platform’s range of variation. Note that in the 5-mm/hr mean precipitation case, the minimum rain rate value for the DMSP was set at 1 mm/hr, not 0 mm/hr. The zero precipitation rate yields a markedly different temporal

variation than non-zero rates. In order to display relative system responses when rain is known to be present, it was decided to use the minimal non-zero value of 1 mm/hr.

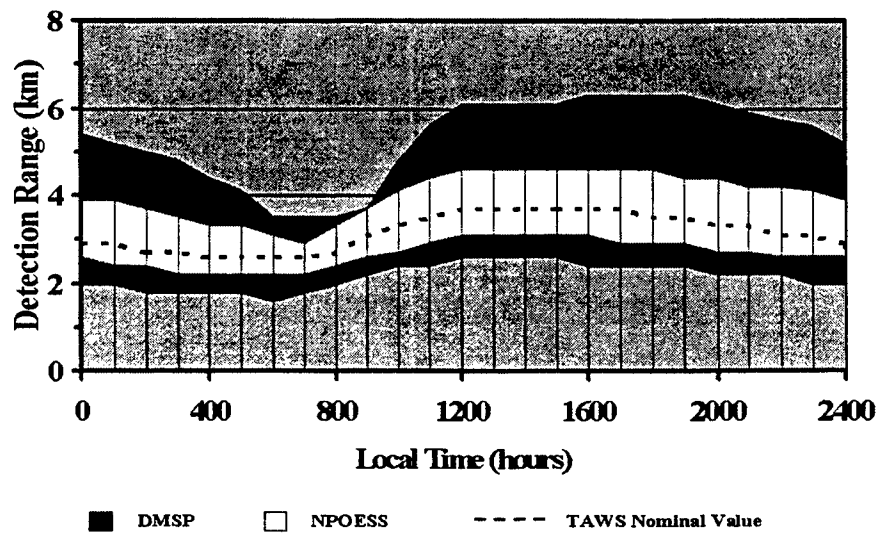


Figure 22. TAWS detection range spread for 5-mm/hr steady precipitation.

The largest disparities between the TAWS/DMSP and TAWS/NPOESS results occur for the light rain (5 mm/hr) results. The DMSP detection range envelope widths vary from 1.5 km to 4 km over the course of the 24-hour period, with the NPOESS results showing a much smaller 0.7- to 1.5-km envelope width over the same period. There is a significant narrowing in the DMSP detection range envelope during the 0800 to 0900 local time period that brings it fairly close to the NPOESS envelope width. This is primarily because of the near equality of the minimum rain rate DMSP and NPOESS detection range results at 0800 and 0900 local time. In fact, the DMSP data have two thermal cross-over events close to 0700 and 0800 for the 1-mm/hr rain rate and 100-ft sensor altitude. This results in a (nearly) zero value ΔT at 0700 and 0800 and an inde-terminate solution for the detection range at these times. The 0600 detection range value was inserted at these “data missing” positions, although the true value is almost certainly lower. The actual 0800-to-0900 narrowing in the DMSP detection range envelope is thus probably more exaggerated than is shown here.

The moderate and high rain rate results show smaller uncertainty envelopes, mainly because of lower fractional uncertainties of the fixed size precipitation rate error. A 0.1-km “quantization” effect at smaller detection range values is also apparent and is caused by the fixed decimal format of the TAWS output values.

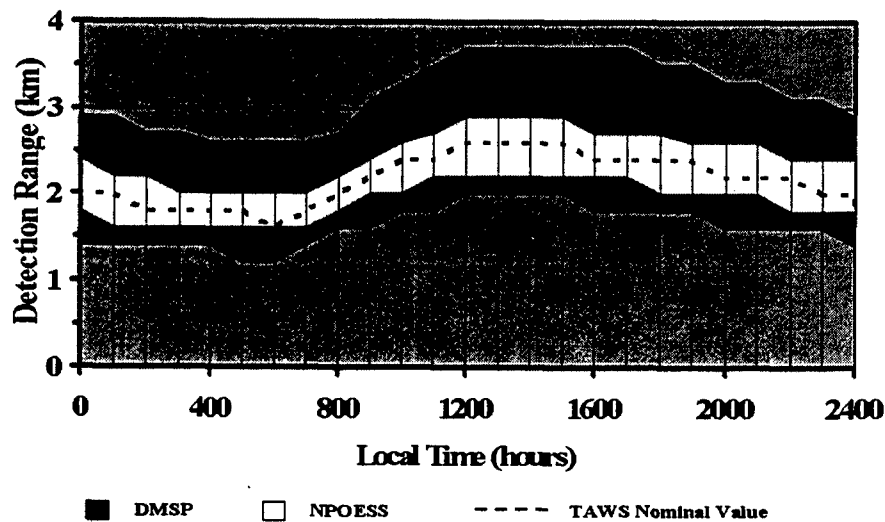


Figure 23. TAWS detection range spread for 10-mm/hr steady precipitation rate.

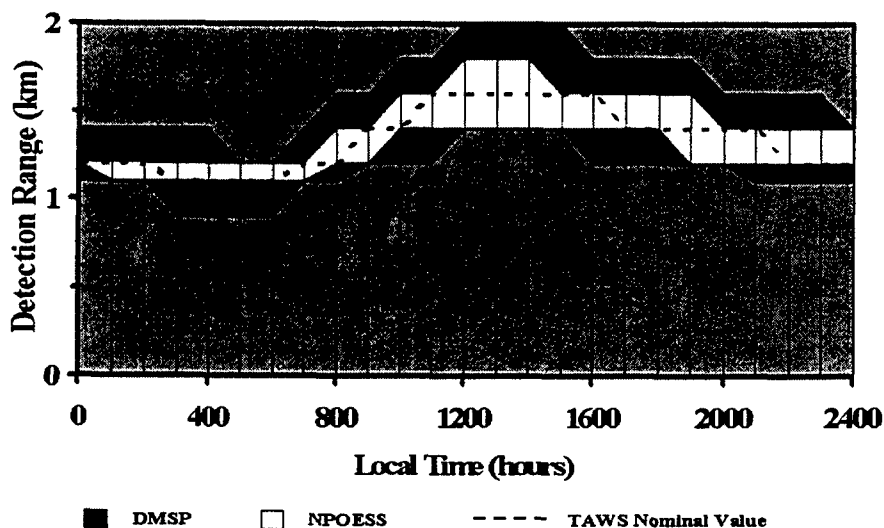


Figure 24. TAWS detection range spread for 20-mm/hr steady precipitation.

5.2 Surface Visibility or Atmospheric Optical Depth

The meteorological visibility near the earth's surface (and within the boundary layer) is another significant input to the TAWS/NOWS models. NPOESS provides sufficient data to assess this property, while DMSP (see, for example, Table 1) does not. If we assume that the boundary (or haze) layer is well mixed, it will have a uniform vertical profile of visible band extinction k_{ext} (km^{-1}) from the surface to the height of the haze layer top Z_H (km). The optical depth τ of the haze layer is then given by $Z_H * k_{\text{ext}}$. The conventional Koschmeider expression for horizontal

meteorological visibility, $V = 3.912/k_{\text{ext}}$, may then be recast in terms of the haze layer height and optical thickness:

$$V(Z_H, \tau) = 3.912 Z_H / \tau . \quad (3)$$

Using the standard error propagation formula for a multivariate function,

$$\sigma_V^2 = \sigma_\tau^2 \left(\frac{\partial V}{\partial \tau} \right)^2 + \sigma_{Z_H}^2 \left(\frac{\partial V}{\partial Z_H} \right)^2 , \quad (4)$$

and the visibility expression from Equation (3), we reach, after some rearrangement, the result:

$$\sigma_V \equiv \frac{V}{Z_H} \sqrt{\left(\frac{\sigma_\tau V}{3.912} \right)^2 + \sigma_{Z_H}^2} . \quad (5)$$

In order to derive a surface visibility from NPOESS measurements, the boundary layer height Z_H AGL and haze layer optical depth τ are determined from the data and inserted into Equation (3). Z_H is effectively the height of the *top* of the capping temperature inversion (over the boundary layer). An NPOESS passive microwave sensor that provides data during both day and night illumination conditions measures the temperature profile required to determine Z_H . Other (surface-based) means may be used to provide this parameter, such as radiosonde data, active lidar/sodar sounding, or diurnal/climatological projection. Here, we will simply assume that the NPOESS temperature profile measurement is used to obtain Z_H and that the uncertainty σ_z is given by the threshold value for vertical resolution in the temperature profile. This value is given in the IORD document (and in Table 2) as an atmospheric pressure increment of 20 mb near the surface or about 0.17 km in height. In practice, σ_z will generally be larger than this value because of the weakness or absence of a distinct capping inversion.

The second parameter required to compute visibility is the total (aerosol plus molecular) optical depth τ . The procedure for retrieval of this parameter from NPOESS data over the entire day is not yet specified in detail in the NPOESS documentation. However, the IORD document does give a threshold value of 0.03 for the uncertainty in the atmospheric optical depth measurement. If we assume that the atmospheric optical depth above the top of the haze layer is well characterized and is nearly invariant, we can use the 0.03 value as an estimate for the haze layer optical thickness σ_τ . We may then assume a small set of visibility examples that might result from application of Equation (3): 2, 5, 10, and 20 km. Further, we might also assume a reasonable set of typical values for the haze layer thickness Z_H : 0.3, 0.5, 1.0, 1.5, 2.0 km. The first two values are characteristic of a thin nighttime boundary layer; the final three are normal for a well-mixed daytime convective boundary layer. We may create a two-dimensional matrix of these parameter values and apply Equation (5) to observe the resulting uncertainties in the derived horizontal visibility. Table 7 displays the results.

Table 7. Visibility uncertainties for different haze layer upper boundary heights Z_H , with the NPOESS threshold resolution for optical depth and temperature profile

Visibility (km)	σ_v (km) $Z_H = 0.3$ km	σ_v (km) $Z_H = 0.5$ km	σ_v (km) $Z_H = 1.0$ km	σ_v (km) $Z_H = 1.5$ km	σ_v (km) $Z_H = 2.0$ km
2	1.3	0.7	0.3	0.2	0.2
5	2.9	1.7	0.9	0.6	0.4
10	6.2	3.7	1.9	1.2	0.9
20	15.3	9.2	4.6	3.1	2.3

Several trends become apparent upon examination of these data. First, the $Z_H = 0.3$ km results have uncertainties that are large fractions of the given visibility (~50 to 80%). This is true simply because the vertical position uncertainty (0.17 km) is comparable to the stated minimum Z_H value. Estimates for horizontal visibility in thin nighttime haze layers (when it is feasible to make them) may thus be expected to have large fractional errors. These estimates will be severely impacted by any failure to approach the stated vertical resolution. Another trend that is evident is the relative constancy of the fractional error σ_v/V for the 2-, 5-, and 10-km visibilities (at any given Z_H). The fractional error for the 20-km visibility is also noticeably larger than the value for the lower visibilities. The invariance of the fractional visibility error at low visibilities is attributable (for the specified values of $\sigma_\tau = 0.03$ and $\sigma_z = 0.17$ km) to the dominance of the “constant” σ_z^2 term on the right-hand side of Equation (5). For example, for $V = 5$ km, the σ_z^2 term is nearly 20 times larger than the term containing σ_τ^2 . However, the latter term varies as the square of the visibility, and the terms become comparable when V increases to 20 km. The enhancement in the fractional error at high visibilities is attributable to the rapid decline in optical depth (signal) in the denominator of Equation (3).

Overall, we may conclude that extraction of horizontal visibility from NPOESS data works best in daytime conditions (i.e., for haze layers exceeding a 0.5-km thickness) and for low visibilities (less than 20 km). We next ask how these results affect NOWS and TAWS detection range results for specific sensor systems. In addition to the NOWS NVG and TAWS IR sensors treated in the previous sections, we will include TAWS results for a TV sensor that primarily operates in daytime conditions. The inclusion of a TV sensor is justified by the fact that it operates in the very parameter space where visibility determination from NPOESS data is most practical.

In the results that follow, we define a quantity ΔR that is equal to one-half the difference between the maximum and minimum detection ranges that are obtained from variations of visibility about the nominal values from the first column of Table 7. Adding and subtracting each σ_v value in Table 7 from the nominal visibility value gives the limits of visibility variation. We use the base NOWS and TAWS environmental scenarios given in Table 3, varying only the meteorological visibility and boundary layer height. The sensor height (100 ft) was low enough that the sensor

position (relative to the top of the boundary layer) would not significantly affect the results. The Nows nighttime results for a common NVG shown in Table 8 indicate only slight impacts because of visibility and boundary layer height. The detection range results appear to be limited by sensor performance in this instance.

Table 8. Nows detection ranges and uncertainties for AN/PVS-7 (third generation), for different haze layer upper boundary heights Z_H at 0100 local time

Visibility (km)	$Z_H = 0.3$ km		$Z_H = 0.5$ km		$Z_H = 1.0$ km		$Z_H = 1.5$ km		$Z_H = 2.0$ km	
	R (km)	ΔR	R (km)	ΔR	R (km)	ΔR	R (km)	ΔR	R (km)	ΔR
	(km)	(km)	(km)	(km)	(km)	(km)	(km)	(km)	(km)	(km)
2	2.9	0.4	2.8	0.3	2.2	0.2	1.8	0.1	1.8	0.1
5	3.5	0.3	3.3	0.2	2.9	0.1	2.8	0.0	2.8	0.0
10	3.7	0.3	3.5	0.2	3.3	0.1	3.1	0.0	3.1	0.1
20	3.9	0.3	3.9	0.1	3.7	0.1	3.5	0.0	3.5	0.1

Daytime detection range performance of a TV sensor for the sample scenario is illustrated in Table 9. In this case, significant uncertainties are seen when the boundary layer height is 0.5 km and lower (for all visibilities). For boundary layer heights 1 km and above, only the 5- and 10-km visibility cases show significant uncertainties (the 20-km visibility is horizon limited from this low altitude vantage point).

Table 10 lists the nighttime and Table 11 the daytime impacts on the TAWS IR sensor for our sample scenario. The nighttime detection ranges appear to be unaffected by the atmosphere (i.e., are system limited) for visibilities 10 km and above. Uncertainties in the detection range appear to be only moderately significant (10% to 20%) for boundary layer heights of 0.5 km and below. The daytime IR results of Table 11 show similar trends, with the nominal detection ranges essentially horizon limited for visibilities of 5 km and above. The detection range uncertainties appear to be significant only for visibilities of 5 km and below and boundary layer heights of 0.5 km and below.

Table 9. TAWS detection ranges and uncertainties for TV sensor (U.S. Air Force Research Laboratory, 2001) for different haze layer upper boundary heights Z_H at 1200 local time

Visibility (km)	$Z_H = 0.3$ km		$Z_H = 0.5$ km		$Z_H = 1.0$ km		$Z_H = 1.5$ km		$Z_H = 2.0$ km	
	R (km)	ΔR	R (km)	ΔR	R (km)	ΔR	R (km)	ΔR	R (km)	ΔR
	(km)	(km)	(km)	(km)	(km)	(km)	(km)	(km)	(km)	(km)
2	2.9	1.2	2.9	0.6	2.9	0.2	3.1	0.1	3.1	0.1
5	6.5	3.7	6.5	2.3	6.7	1.2	6.7	0.9	6.9	0.6
10	13.3	7.4	13.3	5.1	13.6	2.8	13.8	1.7	14.0	1.3
20	19.7	6.8	19.7	2.7	19.7	0.0	19.7	0.0	19.7	0.0

Table 10. TAWS detection ranges and uncertainties for IR sensor (U.S. Air Force Research Laboratory, 2001) for different haze layer upper boundary heights Z_H at 0000 local time

Visibility (km)	$Z_H = 0.3$ km		$Z_H = 0.5$ km		$Z_H = 1.0$ km		$Z_H = 1.5$ km		$Z_H = 2.0$ km	
	R (km)	ΔR	R (km)	ΔR	R (km)	ΔR	R (km)	ΔR	R (km)	ΔR
	(km)	(km)	(km)	(km)	(km)	(km)	(km)	(km)	(km)	(km)
2	10.6	2.5	10.6	1.4	10.6	0.6	10.6	0.4	10.6	0.4
5	14.0	2.2	14.0	1.2	14.0	0.7	14.0	0.5	14.0	0.3
10	15.1	1.1	15.1	0.2	15.1	0.0	15.1	0.0	15.1	0.1
20	15.1	0.8	15.1	0.1	15.1	0.0	15.1	0.0	15.1	0.1

Table 11. TAWS detection ranges and uncertainties for IR sensor (U.S. Air Force Research Laboratory, 2001) for different haze layer upper boundary heights Z_H at 1200 local time

Visibility (km)	$Z_H = 0.3$ km		$Z_H = 0.5$ km		$Z_H = 1.0$ km		$Z_H = 1.5$ km		$Z_H = 2.0$ km	
	R (km)	ΔR	R (km)	ΔR	R (km)	ΔR	R (km)	ΔR	R (km)	ΔR
	(km)	(km)	(km)	(km)	(km)	(km)	(km)	(km)	(km)	(km)
2	13.4	3.5	13.4	2.1	13.4	0.9	13.4	0.6	13.4	0.6
5	19.6	3.0	19.6	1.4	19.6	0.7	19.6	0.4	19.6	0.4
10	19.6	1.0	19.6	0.0	19.6	0.0	19.6	0.0	19.6	0.0
20	19.6	0.1	19.6	0.0	19.6	0.0	19.6	0.0	19.6	0.0

5.3 Cloud Base Height and Cloud Cover

In previous sections, the effect of DMSP and NPOESS imager resolutions on the detection and mapping of cloudy regions was discussed. We now develop a simple two-dimensional cloud mask model to demonstrate how vertical resolution of cloud base height might interact with horizontal resolution of fractional cloud cover. These will then be related to fractional cloud cover effects in TAWS and NOWS detection range predictions.

We limit the discussion to a two-dimensional cloud mask with the realization that three-dimensional cloud fields present a far more complicated general problem. Our task here is to show that *for the approximation of thin inhomogeneous cloud layers*, a few general trends may be deduced. Figure 25 shows the schematic geometry for the thin mask problem. The "cloud mask" here, for the purposes of its use with a TDA, is a two-dimensional function that is derived from satellite cloud imagery. It has a value of 1 when appropriate cloud-clearing algorithms indicate cloudy pixels and 0 when "clear" pixels exist. We will simulate the result of the imaging and cloud-clearing operations with a two-dimensional fractal distribution (Saupe, 1988) that is thresholded to 50% of the maximum pixel value. The cloud mask is at a height h above an observer situated on the surface. A rectilinear cloud mask surface element $dx dy$ is situated at a slant range r_c and at a lateral displacement ρ from the observer.

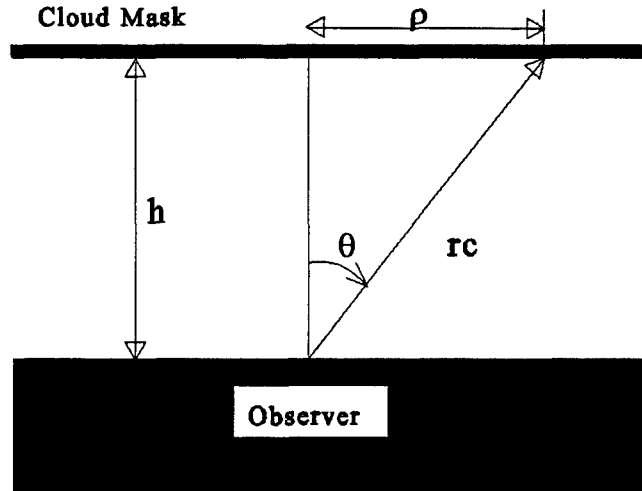


Figure 25. Geometry for computation of surface fractional cloud cover from 2-D cloud mask.

We define the cloud fraction $F(x,y)$ at surface observer position (x,y) as the ratio of the solid angle subtended by cloudy pixels (as seen from the observer's position) to the total solid angle of the hemisphere:

$$F(x,y) = \frac{1}{2\pi} \int_{2\pi} Q(\Omega') d\Omega' , \quad (6)$$

in which $Q()$ is the one-zero cloud mask function that has an implicit (x,y) dependence. If the position of the $dx dy$ area element is given by (x', y') , then from the geometry of Figure 25 we have

$$\begin{aligned} \rho &= \sqrt{(x-x')^2 - (y-y')^2} , \\ r_c &= \sqrt{h^2 + \rho^2} , \\ \cos \theta &= h/r_c , \end{aligned}$$

so that the element of solid angle $d\Omega$ may be expressed as

$$d\Omega = \frac{\cos \theta}{r_c^2} dx dy = \frac{h}{(h^2 + \rho^2)^{3/2}} dx dy .$$

Equation (6) may then be recast in Cartesian coordinates:

$$\begin{aligned} F(x,y) &= \frac{1}{2\pi} \int_{-\infty}^{\infty} \int_{-\infty}^{\infty} Q(x', y') \frac{h}{[h^2 + (x-x')^2 + (y-y')^2]^{3/2}} dx' dy' \\ &= \int_{-\infty}^{\infty} \int_{-\infty}^{\infty} Q(x', y') f(x-x', y-y') dx' dy' , \end{aligned} \quad (7)$$

where the definition

$$f(x, y) = \frac{h}{2\pi(h^2 + x^2 + y^2)^{3/2}} \quad (8)$$

has been made. The right-hand side of Equation (7) is a two-dimensional convolution of the cloud mask function $Q(x,y)$ and the “scanning” function $f(x,y)$. The convolution of the discretely sampled $Q(x,y)$ and $f(x,y)$ functions is achieved by application of the two-dimensional Fourier transform theorem and of a freeware variant of the fast Fourier transform (FFT) (Frigo & Johnson, 1998). We begin a demonstration of this exercise by first showing a sample fractal cloud distribution in Figure 26. The region covered by this distribution (50 km by 50 km) is much larger than that used in the previous sections. The approximate horizontal spatial resolution for this figure is 0.1 km. The cloud density is represented by a 256-level gray scale fractal distribution that has been clipped at the 50% density level. Thus, only the highest densities of the original fractal distribution are represented in the figure. We obtain the cloud mask for this distribution by setting all nonzero values of the distribution density to unity. Figure 27 shows the result of convolving this mask with the scanning function, according to the prescription of Equations (7) and (8) for a mask or “cloud base” height h of 1000 feet (approximately 300 m). The gray scale in Figure 27 has been reduced to eight levels, which correspond to cloud fraction F ranging from 0/8 to 8/8, in increments of 1/8. The figure shows that the convolution closely follows the cloud mask footprint for this low cloud base height. Figures 28 to 30 show the 1000-ft cloud base height convolution results for the NPOESS threshold resolution (0.4 km), DMSP fine resolution (0.55 km), and DMSP smooth resolution 2.7 km), respectively.

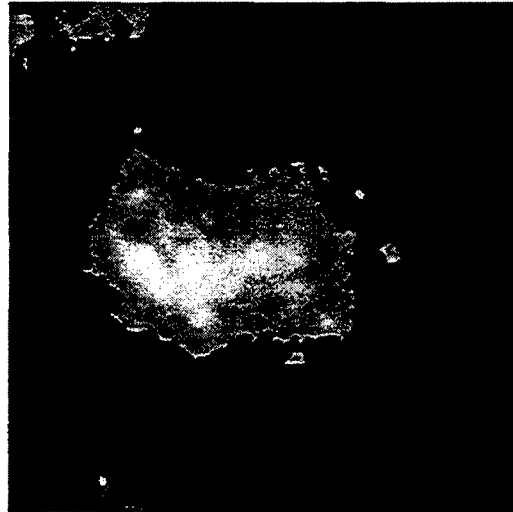


Figure 26. Sample fractal cloud distribution, 50-km by 50-km grid.

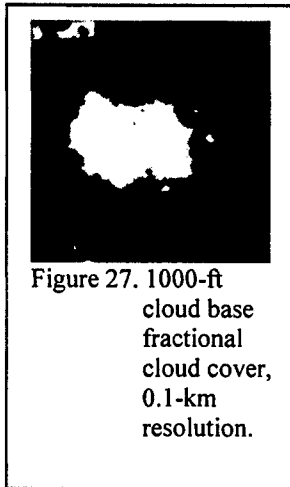


Figure 27. 1000-ft
cloud base
fractional
cloud cover,
0.1-km
resolution.

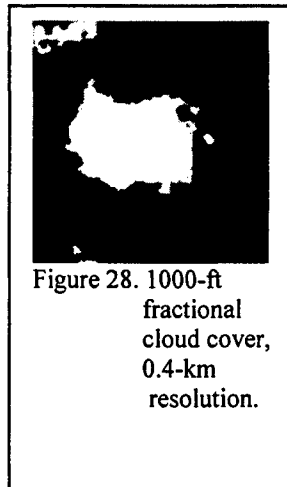


Figure 28. 1000-ft
fractional
cloud cover,
0.4-km
resolution.

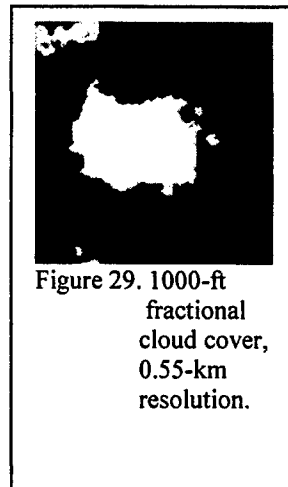


Figure 29. 1000-ft
fractional
cloud cover,
0.55-km
resolution.

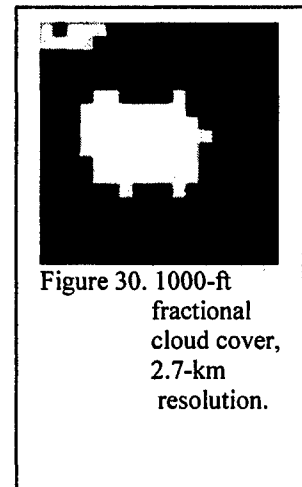


Figure 30. 1000-ft
fractional
cloud cover,
2.7-km
resolution.

Very little difference is seen between the NPOESS threshold and DMSP fine resolution spatial distribution of fractional cloudiness, but the blockiness of the DMSP smooth resolution is apparent. All the lower resolution distributions of overcast-level cloudiness appear to be larger than those for the 0.1-km (original) resolution. This has substantial implications for application of satellite-derived cloud cover data to TDA predictions, because the largest differences for detection ranges occur between overcast and clear conditions. As the height of the cloud mask is increased, the scanning function of Equation (8) broadens and the distributions of fractional cloudiness for the different imaging resolutions become very similar. Figures 31 through 33 show the convolution results for a cloud base height h of 5000 ft (about 1500 m). Figures 34 through 36 represent results for cloud base height h of 10000 ft (about 3000 m). Note that the use of Fourier methods to perform the convolution has introduced aliasing (or “bleed over”) effects into the results. These are more apparent as the scanning function broadens.

The meaning that may be attached to each of the eight intensity levels in Figures 27 through 36 may be illustrated by executing a TDA model and assigning a detection range to each level. For example, the TAWS package may be run for the base scenario of Table 3, with the cloud cover varied from clear to overcast in 2/8 cover increments. The 1000-ft and 5000-ft cloud base heights were run during the “low level cloud” category in TAWS with the stratus/stratocumulus cloud type. The 10,000-ft base height cases were run as “mid-level cloud” nimbostratus cloud types.

For cloud fractions of 4/8 and below, the detection ranges shown in Table 12 are essentially device limited for the local midnight cases and horizon limited for the local noon cases. Higher cloud fractions cause slight reductions in the local midnight detection ranges and significant reductions below the horizon limiting range for the local noon cases. The detection range results apparently have only a weak dependence on cloud base height for the three levels that were sampled. However, Figures 27 through 36 do suggest that the cloud base height has a major effect on the distribution of observed cloud fraction over the surface.

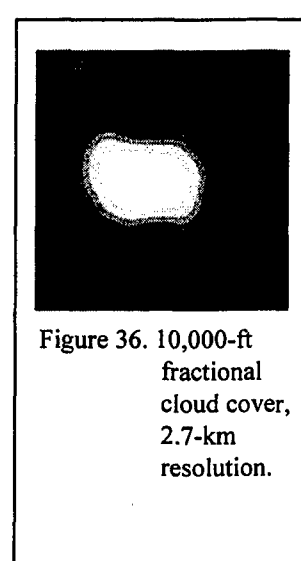
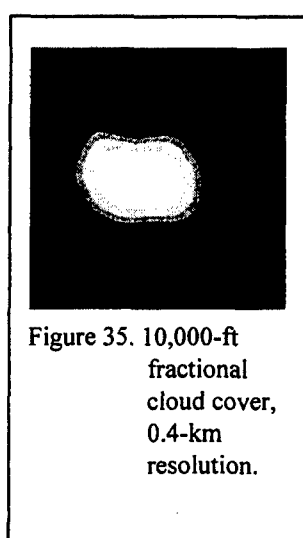
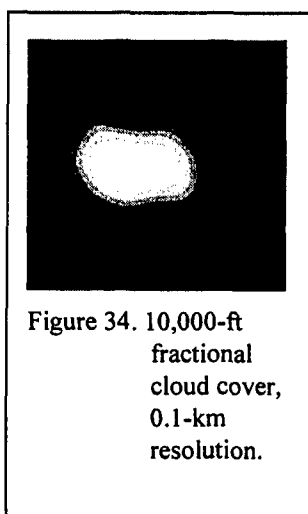
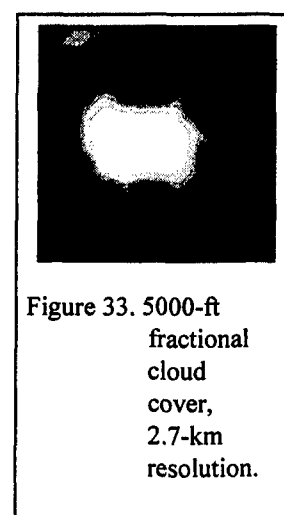
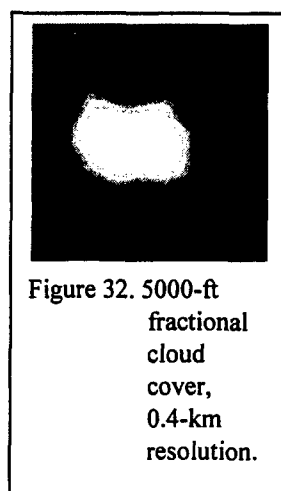
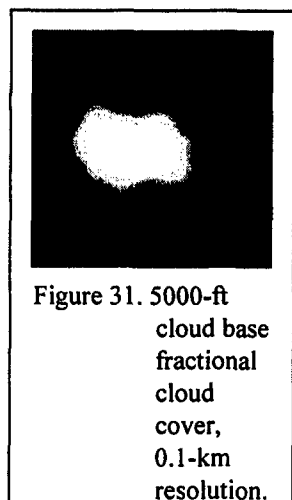


Table 12. Sample comparison of TAWS detection range results for variations of cloud base height and cloud fraction, using the Table 3 base scenario

Cloud Fraction	Cloud Base Height, $h = 1000$ ft		Cloud Base Height, $h = 5000$ ft		Cloud Base Height, $h = 10000$ ft	
	R (km) 0000 Local	R (km) 1200 Local	R (km) 0000 Local	R (km) 1200 Local	R (km) 0000 Local	R (km) 1200 Local
0/8	15.1	19.6	15.1	19.6	15.1	19.6
2/8	15.1	19.6	15.1	19.6	15.1	19.6
4/8	14.7	19.6	14.6	19.6	14.9	19.6
6/8	13.8	15.1	14.0	15.1	14.2	15.1
8/8	12.3	14.9	12.7	15.1	13.3	16.4

The cloud base height reported by a satellite platform thus has an indirect, although significant, effect on TDA model predictions. When combined with imaged cloud cover data, the cloud base height gives us an estimate of the apparent cloud cover that might be used as a TDA input for a near-surface sensor. If the observer/sensor is below the cloud deck, the cloud base height does not (at least for the cases examined) usually have a strong impact on TDA results. However, for very low clouds (e.g., within 2000 feet of the surface), differences in DMSP smooth and NPOESS threshold imaging resolution will be significant for surface targets near the edges of the cloud mass. These differences nearly disappear for cloud base heights of 5000 feet and above. The results of this exercise suggest that threshold value of 2 km for the NPOESS vertical resolution of the cloud base height may be marginal because the transition of the cloud cover footprint from “sharp” to “blurred” occurs at heights on the order of 1 km. This observation should be regarded as tentative because, as noted before, we have based it on the thin mask assumption. In any event, the fact that NPOESS *can* provide an estimate of cloud base height (while DMSP does not) is a step forward from the Army’s TDA application standpoint.

6. Data Latency Issues

The environmental data provided by a satellite platform must traverse some number of communications and data processing links before they become available as usable input to a TDA package. The resulting “data latency period” is defined here as the time interval bound by the satellite platform data acquisition time and the time when the data are available for TDA model ingest. We include “on-board” processing time as part of this time interval. The potential impact of data latency on TDA performance may be appreciated by enumerated examples of environmental conditions that affect TDA predictions and show marked variability in time. For visible and near-IR band sensors, such examples might include transitions between partly cloudy and overcast skies, target movement between regions of differing clutter, transport and diffusion of BIC events, and wind-induced variations of surface visibility. In addition, mid-IR and far-IR sensors might have precipitation start/end times and intensity as serious time-critical determinants of model predictions.

The current versions of the NOWS and TAWS packages are programmed to accept a predicted set of environmental conditions specified by the user for times in the immediate future. For TAWS, these predicted environmental conditions might include mesoscale forecast model results, extrapolations from current conditions reported by surface or airborne observers, or predictions based on remote sensing platform observations. Of course, all these data sources have some degree of data latency and inaccuracy. The primary advantage of the remote sensing approach is that it *can* provide many of the essential TDA model entries in near real time over hostile territory. How closely to “real time” a remote sensor system (such as that on DMSP or

NPOESS) *does* provide these data has a direct effect on the quality of the TDA predictions, as will be seen presently.

As indicated in the impact analysis, one parameter that strongly affects IR sensor performance is precipitation rate. In temperate climates, this quantity is normally very difficult to forecast because of its dependence on many other meteorological conditions (such as air mass evolution and time of air mass arrival over any given surface point), which are also difficult to predict. The effect of precipitation rate data latency may be illustrated with a simple example of a 6-hour rain event that begins at 0600 local time and ends at 1200. The event is a 5-mm/hr “square pulse” superimposed upon the TAWS base scenario of Table 3. The sky is assumed to be clear before and after the event and is assumed to be overcast with low cloud during the event. The hollow dot curve of Figure 37 shows how the detection range results from TAWS vary over the course of the day if the precipitation event is absent. This will be termed the “dry” scenario. The dry scenario is used to illustrate the effect of time lags in data availability at the leading edge of the rain event.

When the precipitation event is included in the scenario, the result shown as the heavy solid curve of detection range versus time in Figure 37 is obtained. Note that the time increment is set at the shortest value available in the TAWS model—15 minutes. The version of TAWS used here allows only 12 time increments when data are reported before and after a given scenario time. Therefore, to cover the 24-hour period of record, the model had to be run at four separate times and the resulting 6-hour “panels” stitched together. This procedure was also followed for the dry scenario of Figure 37. Because the history of the hypothetical rain event is embodied in the heavy solid curve of Figure 37, the following discussion refers to this scenario as the “real” or “actual” scenario. A comparison of the dry and real scenarios reveals that the predicted detection ranges are noticeably different (and somewhat smaller) *after* the end of the rain event. This is because of the normal operation of the TDA model, with its prediction of reduced thermal contrast after periods of rain. A third or “wet” scenario was created to consider the effect of the rainfall (and overcast) event, starting at 0600 and continuing to the end of the 24-hour period. The solid dot curve of Figure 37 shows the detection range results for this scenario, which is used to show data latency effects at the trailing edge of the rain event.

The simulation of data latency effects for the rain event follows a simple set of rules. Because of the unpredictable timing of the precipitation, we assume that only the currently “available” (time-delayed) data are used to extrapolate conditions into the future. We also assume that the TDA model is constantly available to be run to accommodate latest available data. A computer program was created to implement these assumptions and show the resulting disparities (or time-delayed detection range minus real-time detection range “errors”) in model predictions for arbitrary fixed size data latency periods. For each local time value when an error is computed, a “retarded” time equal to the local time minus the latency period was computed. The position of the retarded time relative to the rain event determines whether the beginning or end of the rain event has been observed and which of the dry, wet, or real scenarios is to be used to generate a

prediction at the given time. The difference between this “latent” detection range and the real result is then stored for later display. Figure 38 shows TAWS detection range errors that result from fairly short data latency periods.

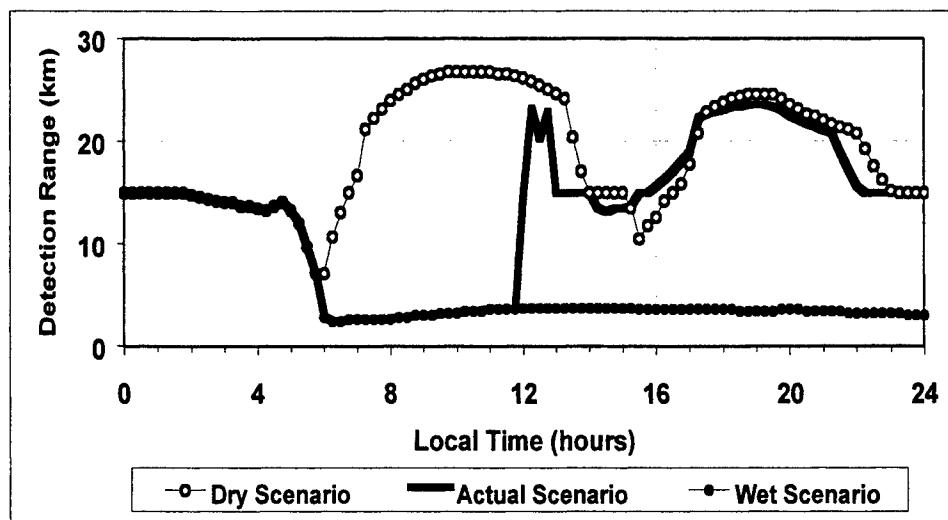


Figure 37. Detection range versus time for the “dry” (no precipitation), “actual” (short precipitation event), and “wet” (extended precipitation event) scenarios.

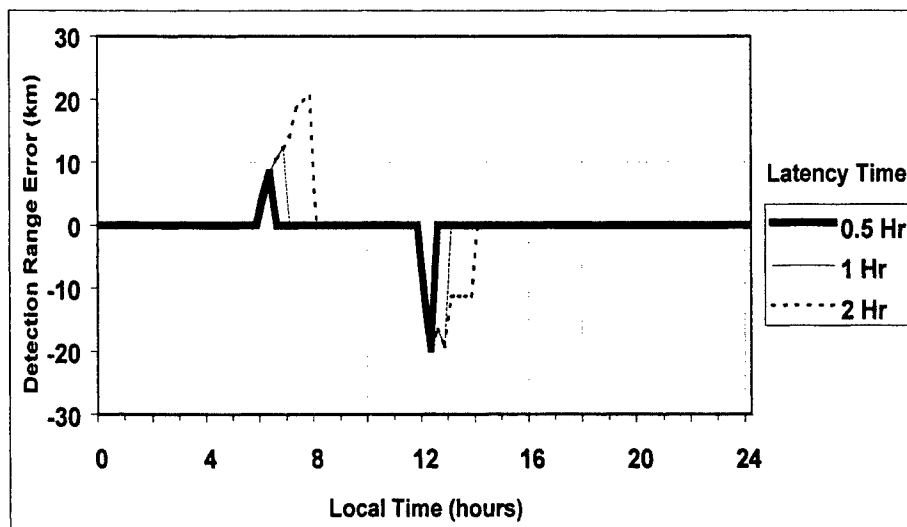


Figure 38. Short period data latency effects for 6-hour rain event beginning at 0600 local time.

Note that the positive amplitude errors in Figure 38 represent latent predictions that are optimistic, i.e., the real-time detection ranges are smaller than the latent ones. Also observe that the maximum range error grows as the latency period lengthens for the onset of the rain event, while the minimum (negative) excursion appears to be independent of latency period (near the end of the rain event). These trends in the error extrema are largely artifacts of where the rain

event is placed in the course of the day. Figure 39 compares data latency effects for medium (3-hour) and long (10-hour) data latency periods. The shorter latency curve has similar characteristics to those in the previous plot, but the 10-hour latency curve is qualitatively different. The long period results show an error with an opposite sign to the medium period at the trailing edge of the rain event pulse. The minimum range error in the long latency curve has about the same amplitude as the medium latency results but occurs 6 to 7 hours later.

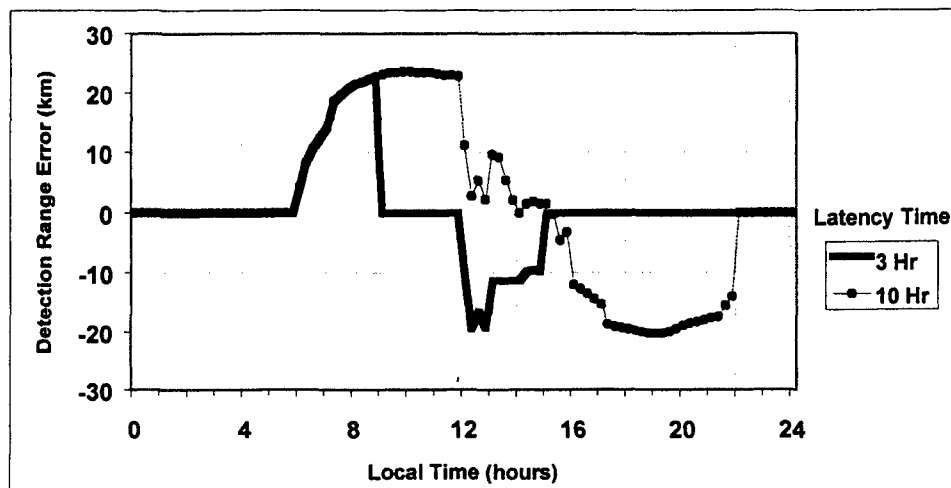


Figure 39. Comparison of medium (3-hour) and long (10-hour) data latency period effects on TAWS detection range estimates.

Figure 40 compares long latency times (6 and 8 hours) that equal and slightly exceed the duration of the rain event. The transition between the short (latency less than or equal to the event duration) and long latency times is particularly evident in this figure.

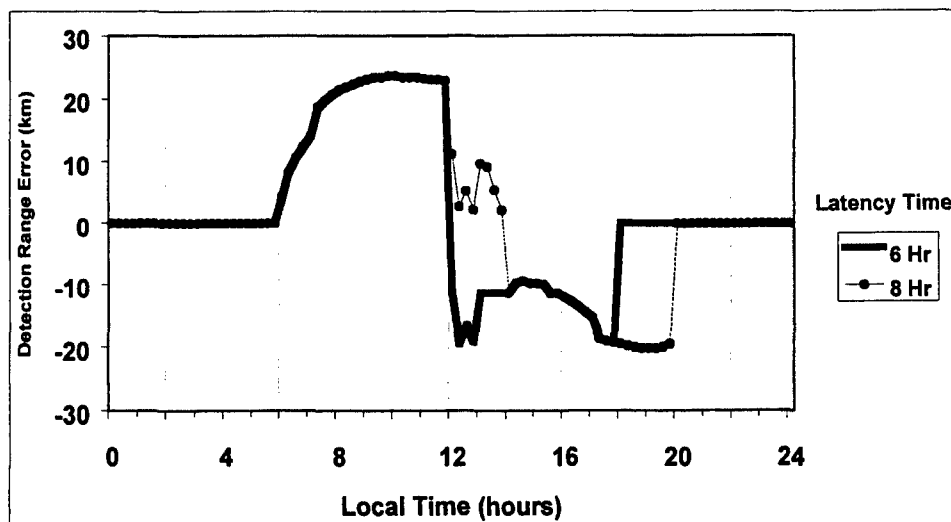


Figure 40. Long period data latency effects on TAWS detection range estimates.

The basic scenario examined here involves a moderate rain rate that persists over a substantial portion of the day. For this situation, it is apparent that any data latency periods longer than 1 hour may lead to substantial detection range errors if ancillary data that refine or complement remotely sensed data are absent. Shorter and more intense rain events will cause even larger errors in TDA performance predictions and will impose stricter limits on acceptable data latency levels. Scenarios in which the rainfall intensity or cloud cover varies markedly over the duration of the event also represent challenges to future efforts at estimation of TDA error because of data latency.

7. Reconnaissance and Combat Asset Effects

When it is desired to search for targets or engage them in combat in a specific region, one quantity that has a bearing on the success at these tasks is the minimum range where the search or targeting sensor can expect to detect targets. Conversely, the maximum range where a sensor on a target platform can detect the platform carrying the attacker's search/targeting sensor can also affect the outcome of a search or attack mission. If the defender's maximum detection range exceeds the attacker's minimum detection range by an appreciable extent, then it may be expected in many individual encounters that the defender will have adequate time to deploy active camouflage (such as screening obscurants), to deploy decoys, to perform evasive maneuvers, or to incapacitate the attacking platform.

For data-denied areas where remote sensing of meteorological conditions by satellite is required, measurement and spatial resolution uncertainties will be associated with measured values of critical TDA input parameters. As seen before, these will translate into detection range estimates and uncertainties for defender and attacker sensor systems.

7.1 Search Asset Effects

The allocation of low altitude search platforms such as unmanned aerial vehicles (UAVs) to establish target positions over a region with defined boundaries is a process that strongly depends on weather conditions. When cloud cover precludes satellite surveillance of a given area and UAV platforms are required to search that area, any precipitation present will limit the detection range available to the UAVs. The detection range degradation will affect the number N of UAV platforms required to survey the region for a given time interval t_{search} or will determine the time interval required to search with a fixed number of platforms. The available precipitation rate over the area may be derived from DMSP or NPOESS data and will be subject to uncertainties analogous to those illustrated before. We may make a crude estimate of required platforms N for a given available search interval t_{search} or, alternatively, t_{search} for a given N under a restrictive set of simplifying assumptions. We assume that the platforms individually execute raster-scan search patterns at a constant altitude, with average ground speed v and with a fractional search

pattern overlap factor α (with $0 \leq \alpha \leq 1$ and $\alpha = 1$ for complete overlap). When multiple platforms are used, we assume that their search intervals coincide in time and do not overlap in space. The precipitation rate (and thus, the detection range r for a given target class) is assumed to be constant over the search period and area. A given platform will then sweep a survey area of $2rv$ per unit time over the search area A . The number of platforms required to perform the reconnaissance mission is then

$$N \equiv \frac{A}{2t_{search}(1-\alpha)rv} \quad (9)$$

If we apply the standard error propagation formula with the form given by Equation (4) and consider only uncertainties in N , t_{search} , and r , we obtain

$$\sigma_N \equiv N \sqrt{\left(\frac{\sigma_t}{t_{search}}\right)^2 + \left(\frac{\sigma_r}{r}\right)^2} \quad (10)$$

for the estimated uncertainty σ_N in the number of required platforms N . The required search time for a given N may then be expressed by rearrangement of Equation (9):

$$t_{search} \equiv \frac{A}{2N(1-\alpha)rv} \quad (11)$$

with the associated uncertainty

$$\sigma_t \equiv t_{search} \sqrt{\left(\frac{\sigma_N}{N}\right)^2 + \left(\frac{\sigma_r}{r}\right)^2} \quad (12)$$

in the required search time. Unlike its meaning in Equation (10), the quantity σ_N might be thought of as a measure of the uncertainty in the number of platforms *available* (e.g., attributable to maintenance or competing mission allocations) rather than *required* to perform the mission.

Practical application of Equations (9) through (12) may require relaxation of any number of the simplifying assumptions given previously, to account for such things as limits on available UAV launching/tracking assets, uneven terrain, attrition because of enemy defenses and system malfunctions, inhomogeneous cloud cover/precipitation, wind fields at platform flight altitudes, and search pattern overlap. We should also note that the finite spatial resolution of the DMSP or NPOESS sensors will result in corresponding uncertainties in the size A of the search area. The purpose of this development is to demonstrate basic differences between results obtained at differing DMSP and NPOESS data resolutions. Thus, the enrichment of the treatment to account for additional environmental variables will be left for future efforts.

The precipitation impact results given in Section 5.1 may be used to construct a simple example that illustrates the implications of this development. Consider a 100-km by 100-km square, flat search area that receives a uniform rain rate over a 24-hour period that we may set to 5, 10, or

20 mm/hr. A notional UAV system considered here might have an average ground speed v of 100 km/h. If the conditions used to construct the results in Section 5.1 are assumed, we may combine the TAWS detection range estimates as functions of rain rate and time, the rain rate measurement uncertainties for DMSP and NPOESS, and Equations (9) through (12) to estimate uncertainties in required assets or search time about a nominal value over the day. The required numbers N of search platforms derived for the three rain rates are shown in Figures 41 through 43, for a search pattern overlap factor of 0.25.

The uncertainty in the number of required platforms for the DMSP measurement accuracy level is significantly larger than that for the NPOESS accuracy at all precipitation rates. The disparity is particularly marked at the 10-mm/hr rain rate. The NPOESS data will thus give us a better idea of the resources required to achieve the mission with a reasonable degree of certainty.

Equations (11) and (12) may also be applied to this scenario and may lead to a similar conclusion with respect to required search time t_{search} . If, for example, the number of available platforms N is 6, then the approximate search time required to search the 100- by 100-km area at the 5-mm/hr rain rate would be as depicted in Figure 44. Note that the criterion for determining a search time given by Equation (11) assumes that the detection range r is invariant *over the search period* t_{search} . This is equivalent to determining a detection range at the beginning of the search period and using it to set a fixed geometry search pattern for the observing platforms. In reality, the search periods can be long enough (several hours) that the detection range may well vary significantly during the search. These results are coarse, but they do at least provide a first order estimate for anticipated surveillance times during adverse conditions.

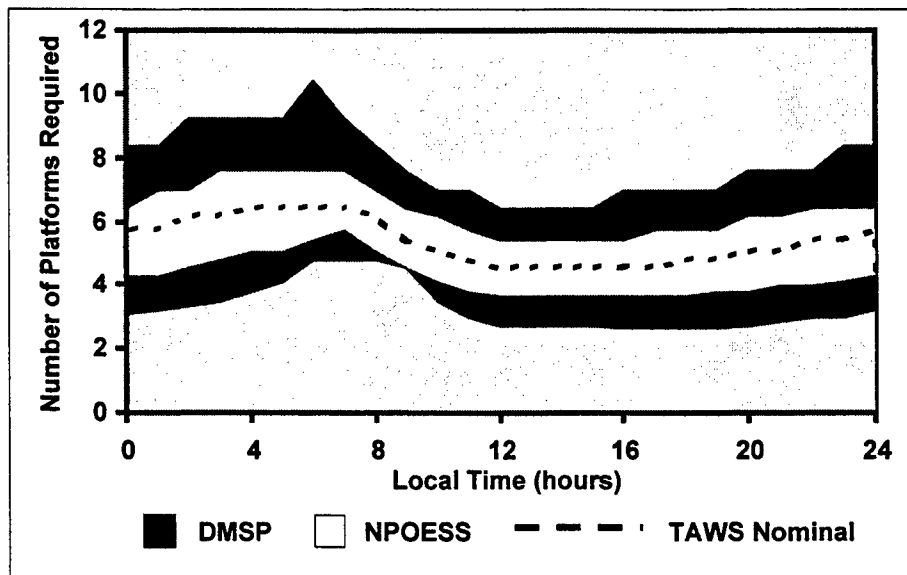


Figure 41. Estimated number N of search platforms required to search a 100- by 100-km area in 4 hours, for a 5-mm/hr steady rain.

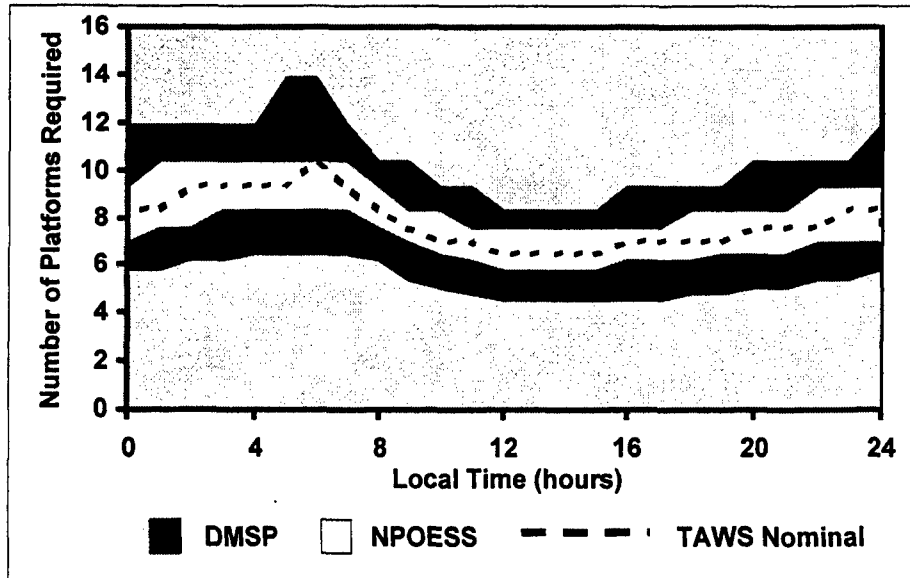


Figure 42. Required number of search platforms for a 10-mm/hr rain rate.

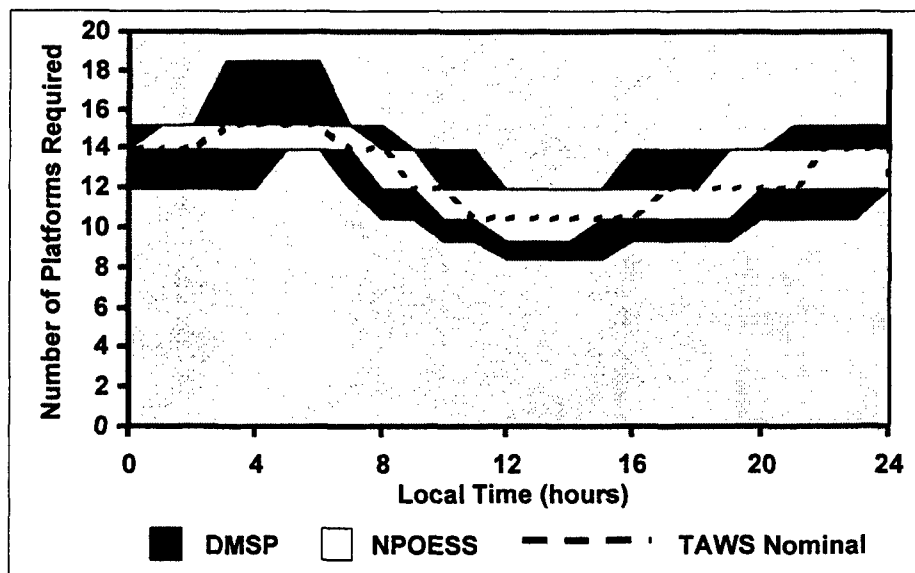


Figure 43. Required number of search platforms for a 20-mm/hr rain rate.

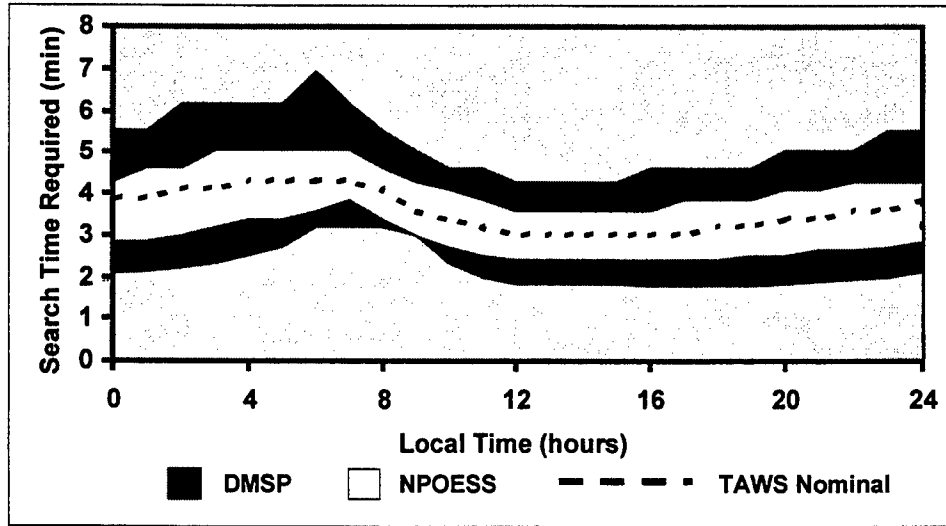


Figure 44. Estimated search time for a 100- by 100-km area with six observing platforms at a 5-mm/hr rain rate.

A more refined estimate of required search assets or time assumes continuous variation of the detection range r with time. An alternate view of this assumption is that the observing platforms are allowed to adapt their search patterns as detection conditions change. The time-invariant expression of Equation (11) may therefore be modified to assume the differential form

$$\frac{dA}{dt} = 2N(1-\alpha) v r(t) \quad (13)$$

This may be integrated over the search area A and between search times t_o and $t_o + t_{search}$ to yield the expression

$$\int_0^A dA' = 2N(1-\alpha) v \int_{t_o}^{t_o + t_{search}} r(t) dt \quad (14)$$

Performing the area integration and rearranging, we get the result

$$\frac{2N(1-\alpha)v}{A} \int_{t_o}^{t_o + t_{search}} r(t) dt = 1 \quad (15)$$

which can be evaluated numerically and incrementally to provide an estimate of the search time t_{search} for a given search period starting time t_o . A computer program was devised to perform this operation through cubic splines to the TAWS-output detection range function $r(t)$ and Romberg integration. The results for the environmental conditions specified earlier in this section and $N = 6$ observing platforms are given in Figures 45 through 47 for the three rain rates.

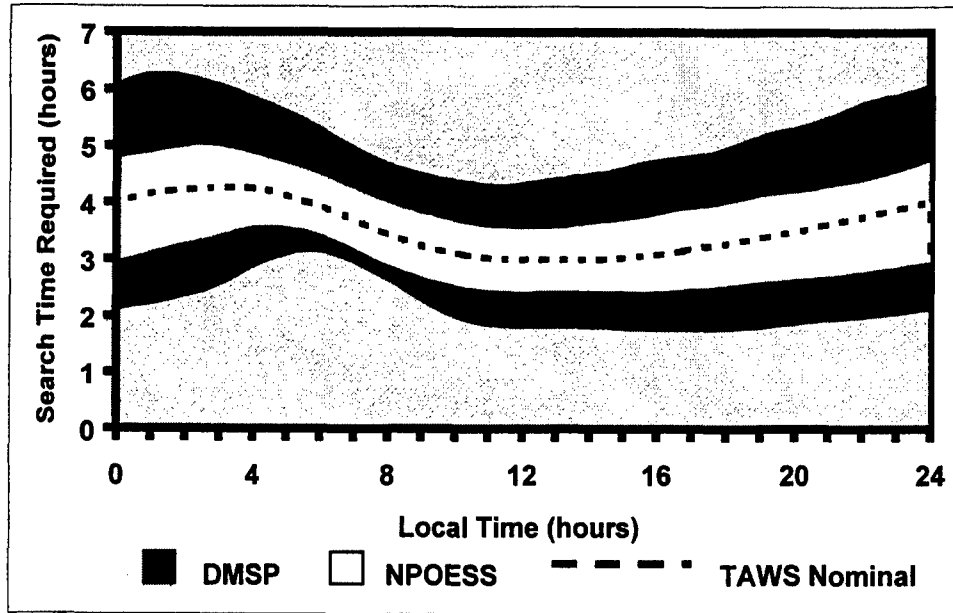


Figure 45. Comparison of DMSP and NPOESS refined estimated search time uncertainties for a 5-mm/hr rain rate.

The search times displayed in Figures 45 through 47 may be regarded as “adaptive” because they represent scenarios where the observing platforms respond to diurnal changes in detection range and modify their search patterns accordingly. Also note, in a comparison of Figures 44 and 45, that features in the search time curves are shifted to an earlier time of day in the adaptive search pattern scenario of Figure 45 relative to those in the fixed pattern scenario of Figure 44.

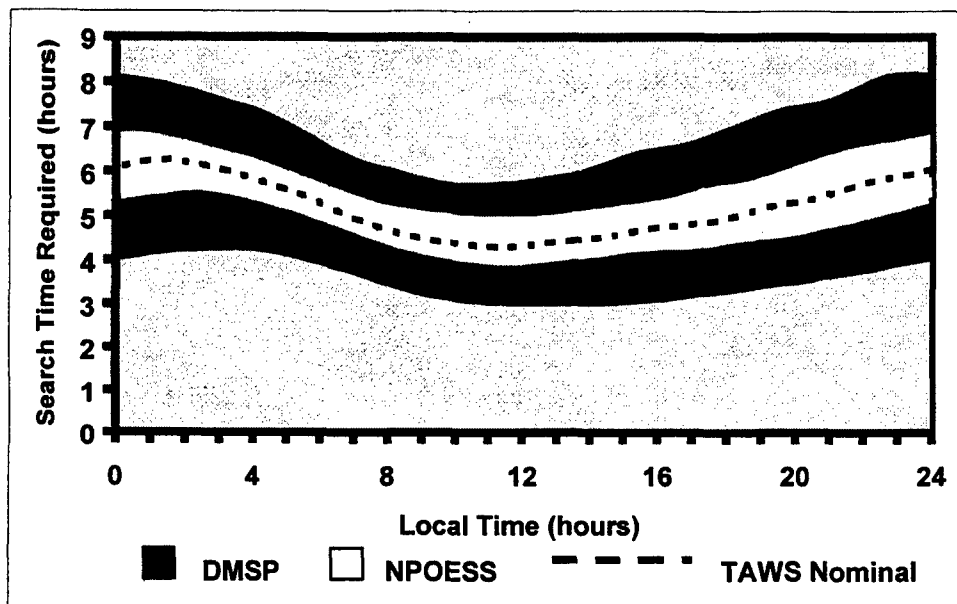


Figure 46. DMSP and NPOESS refined search time comparison for a 10-mm/hr rain rate.

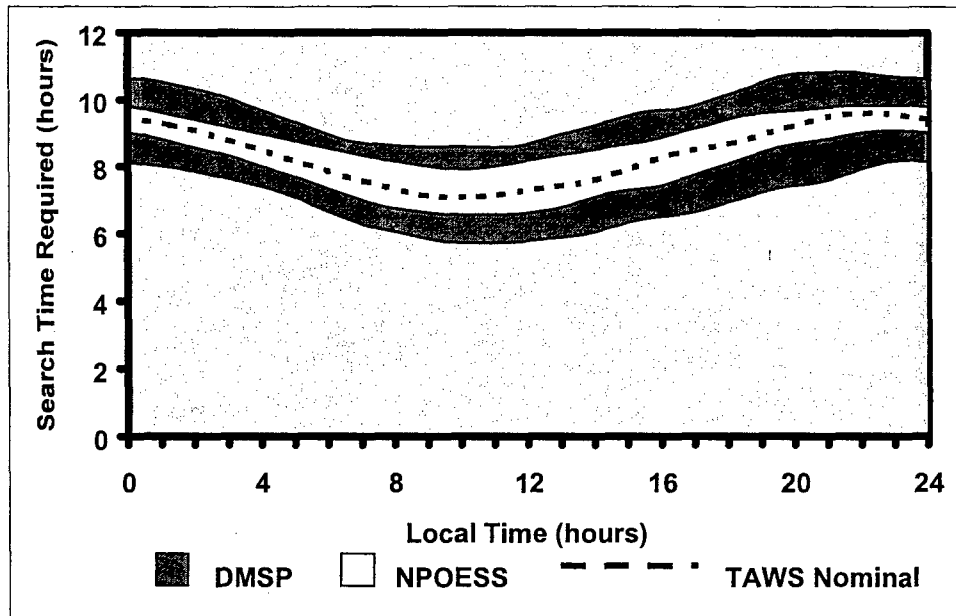


Figure 47. DMSP and NPOESS refined search time comparison for a 20-mm/hr rain rate.

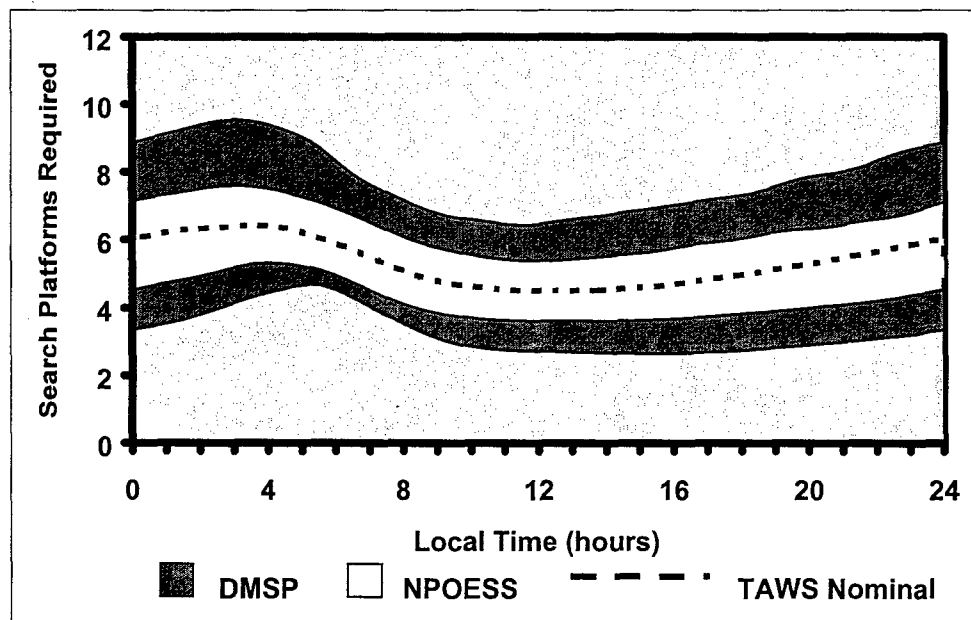


Figure 48. DMSP and NPOESS uncertainties in search platform requirements for search of a 100- by 100-km area in 4 hours, 5-mm/hr rain rate.

The condition given by Equation (15) may be rearranged to yield the number N of platforms required to perform a search over time t_{search} , starting at time t_0 :

$$N(t_0) = \frac{A}{2(1-\alpha) v \int_{t_0}^{t_0 + t_{search}} r(t) dt} \quad (16)$$

Unlike the implicit solution for t_{search} given as the limit of the integral in Equation (15), the solution for N given in Equation (16) is explicit. If the scenario conditions for the 5-mm/hr rain rate already stated are used, the number of required platforms over the course of the day (for a 4-hour search period) is displayed in Figure 48. These results may be compared with those shown in Figure 41. Like the curves for search time versus time of day, general features in the platform requirement curves shift to an earlier time of day for the adaptive search mode.

7.2 Combat Attrition Effects

The basic Lanchester equations for modern warfare used in force-on-force attrition modeling may be stated as (Taylor, 1981)

$$\begin{aligned}\frac{dx}{dt} &= -ay, \quad \text{with} \quad \frac{1}{a} = t_{aXY} + \frac{1}{v_Y P_{SSKXY}} \\ \frac{dy}{dt} &= -by, \quad \text{with} \quad \frac{1}{b} = t_{aYX} + \frac{1}{v_X P_{SSKYX}}\end{aligned}\tag{17}$$

in which x and y are the force levels of the combatants at any given time t , t_{aXY} (t_{aYX}) is the mean acquisition time of target X (Y) for shooter Y (X), v_Y (v_X) is the firing rate for shooter Y (X), P_{SSKXY} (P_{SSKYX}) is the probability for a single-shot kill on target X (Y) by shooter Y (X), and the coefficient a (b) is a measure of the effectiveness of shooter Y (X) in reducing target X (Y). Although many other forms for the force-on-force attrition relations are available in the literature, we will focus on the basic Lanchester relations because the essential impact of acquisition time is clearly illustrated.

If the Lanchester attrition rate coefficients a and b are assumed to be constant during the course of the engagement, then Equation (17) leads to the Lanchester square law (Taylor, 1981):

$$b(x^2 - x_0^2) = a(y^2 - y_0^2),\tag{18}$$

in which x_0 and y_0 are the initial force levels for X and Y . Taylor points out that these initial values and the Lanchester coefficient ratio a/b have a number of important impacts on the outcome of the X/Y engagement. For example, in a fight-to-the-finish scenario in which X wins the engagement, it is necessary (from Equation (18)) to have the condition $(x_0/y_0) > (a/b)^{1/2}$. The relative fire effectiveness ratio $\eta = a/b$ plays a pivotal role not only in the linear system of Equation (17), but in other, nonlinear, attrition formulations as well. However, we will focus on the explicit dependence of the a and b coefficients on the t_{aXY} and t_{aYX} acquisition times given in Equation (17):

$$a = \left(t_{aXY} + \frac{1}{v_Y P_{SSKXY}} \right)^{-1},\tag{19}$$

$$b = \left(t_{aYX} + \frac{1}{v_X P_{SSK YX}} \right)^{-1}.$$

The standard propagation of errors formulation used here may be applied under the assumption that σ_v and σ_P are zero:

$$\begin{aligned} \sigma_\eta &= \eta \sqrt{\left(\frac{\sigma_a}{a} \right)^2 + \left(\frac{\sigma_b}{b} \right)^2}, \\ &= \eta \sqrt{a^2 \sigma_{t_{aXY}}^2 + b^2 \sigma_{t_{aYX}}^2}, \end{aligned} \quad (20)$$

in which the intermediate results $\sigma_a = a^2 \sigma_{t_{aXY}}$ and $\sigma_b = b^2 \sigma_{t_{aYX}}$ derived from Equation (19) have been employed.

The acquisition times t_{aXY} and t_{aYX} may be determined by application of the NVESD search model (Howe, 1993) and the appropriate TDA model. The mean acquisition time τ_{FOV} (in seconds) for a target within a sensor FOV for an ensemble of observers is given by

$$\tau_{\text{FOV}} = \begin{cases} \frac{3.4}{P_\infty} & \text{for } P_\infty \leq 0.9 \\ 6.8 \frac{(N_{50})_D}{N} & \text{for } P_\infty > 0.9 \end{cases} \quad (21)$$

in which P_∞ is the fraction of the ensemble of observers that can eventually find the target, given an unlimited amount of time, N is the number of resolvable cycles across the target-critical dimension for the given environmental conditions and target range, and $(N_{50})_D$ is the number of resolvable cycles across the target-critical dimension required for 50% of the observer population to acquire the target for a particular target and clutter level combination. The asymptotic probability P_∞ is given as

$$\begin{aligned} P_\infty &= \frac{[N / (N_{50})_D]^E}{1 + [N / (N_{50})_D]^E}, \\ E &= 2.7 + 0.7 \left[\frac{N}{(N_{50})_D} \right]. \end{aligned} \quad (22)$$

The resolvable cycle quantities N and $(N_{50})_D$ used here are not direct output of the GUI version of the TAWS 2.2 model used in the preparation of this report. The quantity N is explicitly available within the body of the TAWS code, but $(N_{50})_D$ may be derived from user input for clutter level

and target type. Because an alternate sensor performance model has been proposed for a TAWS upgrade (Shirkey, Sauter, & Cormier, 2001), it may be premature to modify the TAWS code to provide the $N/(N_{50})_D$ ratio that is required in the development. With the equivalence between τ_{FOV} and either t_{aXY} or t_{aYX} , it is then possible to derive a , b , σ_a , and σ_b for the combatant force elements. In general, the sensors used by X and Y will be different and thus, t_{aXY} will not equal t_{aYX} . The modified version of TAWS (or NOWS) will therefore need to be exercised for both X and Y's sensor-target combinations.

8. Summary and Conclusions

A survey of parameters for sensors modeled in the NOWS and TAWS TDA packages revealed that a small set of environmental variables significantly influenced detection range results for the chosen scenarios. Table 13 summarizes these results.

Table 13. Summary of significant parameter main effect and interaction impacts

TDA Model / Sensor Type	Significant Main Effects	Significant Interactions
NOWS / NVG	Clutter level, background type	Illumination x Clutter Clutter x Background type Clutter x Boundary layer height Clutter x BIC
TAWS / IR (sparse/dense vegetation)	Precipitation intensity, cloud cover, BIC	Clutter x Cloud cover (WFOV) Season x Cloud cover Precipitation x BIC (NFOV) Precipitation x Clutter
TAWS / IR (sparse/dense vegetation)	Precipitation intensity, cloud cover, background type, BIC	Background x Season Background x Precipitation Background x Cloud cover Season x Cloud cover Precipitation x BIC

The NPOESS threshold resolution provides superior spatial and parametric characterization in comparison to that provided by the DMSP for several environmental parameters. The most important of these from the Army standpoint are precipitation rate and cloud cover for IR and NVG sensors and to a lesser degree, meteorological visibility for visible band TV sensors. An example that demonstrates the superior NPOESS resolution may be seen in the portion of detection range uncertainties in TAWS IR results attributable to DMSP/NPOESS rain rate measurement errors in the sample scenario described. Table 14 summarizes the essential results of this comparison.

Table 14. Comparison of approximate TAWS IR detection range errors attributable to DMSP and NPOESS measurement uncertainties

Nominal Precipitation Rate	DMSP Detection Range Error	NPOESS Detection Range Error
5 mm / hr	1.5 km	0.5 km
10 mm / hr	0.75 km	0.25 km
20 mm / hr	0.25 km	0.1 km

The calibrated radiometric data from the VIIRS sensor and the finer frequency coverage and spatial resolution of the microwave-band CMIS and CrIS sensors on NPOESS will make certain parameters (such as surface visibility, boundary layer height, and cloud base height) available at resolutions of practical use in Army TDA applications. Extraction of surface visibility from the NPOESS data appears to be most practical for the combination of the daytime boundary layer (with thicknesses exceeding 0.5 km) and low visibility (meteorological visibilities of less than 20 km). The higher horizontal resolution NPOESS imagery should also be superior to DMSP for detecting range estimates at surface points near the edges of low cloud masses (with cloud base heights on the order of 1 km AGL).

The rapidly varying rain scenario outlined here for the IR sensor illustrates that data latencies that exceed on the order of 0.5 hour or more may seriously degrade the accuracy of TDA detection range estimates. If operations during transient marginal weather conditions such as broken heavy cloudiness or localized rain showers are anticipated, it would be wise to assume that sensor performance predictions attributable solely to satellite observations would simply provide a range of possibilities. More precise estimates could be secured (with some difficulty) by data latency times being kept below 0.5 hour and the mission time over target being synchronized with satellite overpass times for the target area. Another possibility is the use of airborne weather radar to more precisely estimate rain rate or cloud cover over the target in near real time. The use of data from a polar orbiting satellite platform is still useful in this latter case, because the defining range of sensor performance predictions may be determined ahead of time with some degree of confidence. Near real-time mission go/no-go or approach route decisions could then be rendered more accurately and more rapidly.

A cursory assessment of target search times indicates that a more reliable estimate of required search assets or times may be achieved through the use of NPOESS-resolution data. A rough estimate is that the uncertainty in the NPOESS predictions will be 2 to 3 times smaller than comparable DMSP-resolution predictions.

If the war gaming community wishes to include the effect of supporting satellite weather observations in combat attrition scenarios, it will be important to modify the current TDA inventory to provide the explicit input required to control the combat exchange equations. The estimation of the impact of spatial or parameter resolution on the attrition of combat assets will likely have to await the coupling of a particular TDA to a particular war game simulation.

Obviously, the results given here for spatial resolution and parameter impacts are not comprehensive. However, they are entirely adequate to demonstrate substantial improvements in data quality (in comparison to that presently available from DMSP) when the threshold NPOESS resolutions are considered.

This study has also pointed out some limitations of the TDA implementations that reduce their utility to Army users. In particular, the treatment of BIC effects could be made more sophisticated by at least enabling the user to specify proportions of obscurant aerosol types and to specify absolute concentrations. The current version of TAWS allows only a single "average" mixture of BIC components at a single absolute concentration. One may explicitly consider the effects of three inventory smokes (white phosphorous, fog oil, and hexachloro-ethane) in the current version of TAWS but only by substituting these (one at a time) for the background haze aerosol. Future studies that couple TAWS with satellite data or battlefield obscurant transport and diffusion models will be more practical if BIC components may be easily and independently added to environmental scenarios in TAWS.

Capability to output resolvable cycle results for given sensor-target combinations should be added to TAWS. This will make application of TAWS results to combat attrition models a feasible proposition.

Later releases of TAWS may address the problem of displaying model results for a full 24-hour period at the highest time resolution. Currently, the user must run the code several times in order to cover the entire day at the 15-minute time resolution.

Detection range impacts attributable to precipitation intensity could not be directly examined for the NOWS NVG cases. A more explicit treatment of rain/snow rate impacts in NOWS (or its embedded successor in TAWS) might thus prove useful for Army users. This would also permit extension of the IR sensor studies of data latency effects because of rain or snow to TV and NVG sensor types.

A few properties of the background surface adjacent to the target should be investigated further. These include the effects of near-surface soil moisture and large scale clutter in the vicinity of large targets. Soil moisture effects on detection range were somewhat smaller than anticipated in the results discussed previously. Different target types, sensor selections, or soil types may produce more significant soil moisture effects than those observed here. The nominal spatial resolution of polar orbiting platforms makes a direct assessment of background clutter practical for fairly large targets. Indirect assessment of smaller scale surface clutter may be possible when large scale regions of characteristic clutter features (such as clumps of vegetation in desert areas) are identified and their state (e.g., wet, growing, snow covered, etc.) is characterized.

A more detailed (3-D) treatment of the interaction of satellite imaging resolution, cloud cover, cloud base height, and TDA detection range estimates in the vicinity of cloud boundaries could be used to refine the results of the simplified 2-D evaluation given. The 3-D treatment will be

especially significant for cases when the apparent angle between the sun and the satellite platform or the angle between the satellite and the local zenith (as seen from the target location) is large. In that event, the distribution of cloud shadows over the target scene or the apparent level of cloudiness may be much different from those deduced from a simple 2-D cloud mask scheme.

9. References

- Box, G.E.P., Hunter, W.G., and Hunter, J.S. (1978). *Statistics for experimenters: An introduction to design, data analysis, and model building*. New York: John Wiley and Sons.
- Cormier, R.V. (28-29 March 2000). *NOWS Sensitivity Study*, presentation at the Weather Impacts Decision Aid meeting, Hurlburt Field, FL.
- Frigo, M., and Johnson, S.G. (1998). "FFTW: An adaptive software architecture for the FFT," *ICASSP Conference Proceedings*, 3, 1381-1384.
- Gouveia, M. (1997). *Night Vision Goggles Operations Weather Software (NOWS)* (Technical Report PL-TR-9702151; AD B233265). Hanscom AFB, MA: Phillips Laboratory.
- Howe, J.D. (1993). "Electro-optical imaging system performance prediction," In *The Infrared and Electro-Optical Systems Handbook (U)*, Volume 4, M.C. Dudzik, Ed., Infrared Information Analysis Center and SPIE Optical Engineering Press.
- Johnson, K., A. Curran, D. Less, D. Levanen, E. Marttila, T. Gonda, Jack, and Jones, "MuSES: A New Heat and Signature Management Design Tool for Virtual Prototyping," *Proceedings of the Ninth Annual Ground Target Modeling and Validation Conference*, Houghton, MI (August 1998).
- Joint Agency Requirements Group (JARG) (2000). *Draft integrated operational requirements document (IORD) 1A*. Web site: http://npocsslib.ipo.noaa.gov/Req_Doc/IORD_draft_1a.pdf.
- Keegan, T.J. (1990). *EOTDA Sensitivity Analysis* (Technical Report GL-TR-90-0251 (II)). Hanscom AFB, MA: U.S. Air Force Geophysics Laboratory.
- Saupe, D. (1988). Algorithms for random fractals. In *The Science of Fractal Images*, H.O. Peitgen and D. Saupe, Eds., New York: Springer-Verlag.
- Shirkey, R.C., Sauter, B.J., and Cormier, R.V. (2001). *Weather Effects on Target Acquisition Part 1: Sensor Performance Model and Infrared Algorithms* (Technical Report ARL-TR-821). White Sands Missile Range, NM: U.S. Army Research Laboratory.
- Taylor, J.G. (1981). *Force-on-force attrition modeling*. Arlington, VA: Military Applications Section, Operations Research Society of America.
- Touart, C.N., Gouveia, M.J., DeBenedictis, D.A., Freni, J.M.L., Halberstam, I.M., Hilton, P.F., Hodges, D.B., and Hopes, D.M. (1993). *Electro-optical tactical decision aid (EOTDA) user's manual, version 3, technical description, appendix a* (Technical Report PL-TR-93-2002 [II]; AD B171600L). Hanscom AFB, MA: Phillips Laboratory.
- U.S. Air Force Research Laboratory (2001). *TAWS Version 3.0 Sensors*, (CLASSIFIED).
- U.S. Army CECOM (1995). *Acquire range performance model for target acquisition systems, version 1 user's guide* (report). Ft. Belvoir, VA: U.S. Army CECOM Night Vision and Electronic Sensors Directorate.

10. Acronyms

AGL	above ground level
ARL	Army Research Laboratory
AVHRR	advanced very high resolution radiometer
BIC	battlefield-induced contaminants
CECOM	Communication and Electronics Command
CFLOS	cloud-free line of sight
CMIS	conical microwave imager/sounder
CrIS	cross-track infrared sounder
DMSP	Defense Meteorological Satellite Program
DOS	disk operating system
EDR	environmental data record
EOS AM-1	earth-orbiting system AM-1 passage
EOTDA	electro-optical tactical decision aid
FFT	fast Fourier transform
FWHM	full width at half maximum
GUI	graphical user interface
IOD	integrated operational requirements document
IR	infrared
Landsat	land satellite system
LOS	line of sight
MODIS	moderate resolution imaging spectro-radiometer
MuSES	multi-service electro-optic signature
NOAA	National Oceanic and Atmospheric Administration
NFOV	narrow field of view
NOWS	NVG operations weather software
NPOESS	national polar-orbiting operational environmental satellite system
NVESD	Night Vision and Electronic Sensors Directorate
NVG	night vision goggles
OLS	operational line scan system
OS	operating system
PMT	photo multiplier
SPOT	<i>Satellite Pour l'Observation de la Terre</i>
SSM/I	special sensor microwave imager
SSM/T-1	special sensor atmospheric temperature sounder

SSM/T-2	special sensor microwave water vapor profiler
TAWS	target acquisition weather software
TDA	tactical decision aid
TV	television
UAV	unmanned aerial vehicle
VIIRS	visible/infrared imager/radiometer suite
WFOV	wide field of view

REPORT DOCUMENTATION PAGE				Form Approved OMB No. 0704-0188	
<p>Public reporting burden for this collection of information is estimated to average 1 hour per response, including the time for reviewing instructions, searching existing data sources, gathering and maintaining the data needed, and completing and reviewing the collection information. Send comments regarding this burden estimate or any other aspect of this collection of information, including suggestions for reducing the burden, to Department of Defense, Washington Headquarters Services, Directorate for Information Operations and Reports (0704-0188), 1215 Jefferson Davis Highway, Suite 1204, Arlington, VA 22202-4302. Respondents should be aware that notwithstanding any other provision of law, no person shall be subject to any penalty for failing to comply with a collection of information if it does not display a currently valid OMB control number.</p> <p>PLEASE DO NOT RETURN YOUR FORM TO THE ABOVE ADDRESS.</p>					
1. REPORT DATE (DD-MM-YYYY) MARCH 2003		2. REPORT TYPE FINAL		3. DATES COVERED (From - To)	
4. TITLE AND SUBTITLE Enhancement of Army Operational Capabilities with the Use of NPOESS Data				5a. CONTRACT NUMBER	
				5b. GRANT NUMBER	
				5c. PROGRAM ELEMENT NUMBER	
6. AUTHOR(S) O'Brien, S. G. (NMSU); Shirkey, R. C. (ARL); Sauter, B.J. (ARL)				5d. PROJECT NUMBER	
				5e. TASK NUMBER	
				5f. WORK UNIT NUMBER	
7. PERFORMING ORGANIZATION NAME(S) AND ADDRESS(ES) U.S. Army Research Laboratory Computational & Information Sciences Directorate White Sands Missile Range, NM 88002-5501				8. PERFORMING ORGANIZATION REPORT NUMBER ARL-TR-2789	
9. SPONSORING/MONITORING AGENCY NAME(S) AND ADDRESS(ES) U.S. Army Research Laboratory 2800 Powder Mill Road Adelphi, MD 20783-1145				10. SPONSOR/MONITOR'S ACRONYM(S)	
				11. SPONSOR/MONITOR'S REPORT NUMBER(S) ARL-TR-2789	
12. DISTRIBUTION/AVAILABILITY STATEMENT Approved for public release; distribution unlimited.					
13. SUPPLEMENTARY NOTES					
14. ABSTRACT <p>When compared with the current Defense Meteorological Satellite Program (DMSP) system, the proposed National Polar-Orbiting Operational Environmental Satellite System (NPOESS) will provide superior spatial and parametric resolution for environmental parameters that are significant in Army operations. Two tactical decision aid models used by the Army, the Night vision goggles Operations Weather Software (NOWS) and the target Acquisition Weapons Software (TAWS), were used to evaluate the degree of improvement that is possible in target acquisition predictions because of the enhanced accuracy of NPOESS measurements. Before performing this evaluation, we first identified the most significant parameters for selected night vision goggle and infrared low altitude sensors during a few environmental scenarios. We then examined the relative impact that several of these environmental parameters had on the detection range predictions from the NOWS and TAWS models during the selected scenarios. The most significant parameters were examined in detail to display the quantitative effect that the increased NPOESS resolution has on the uncertainty in NOWS/TWAS detection range estimates. We also examined the effect that delays in supplying an environmental input to NOWS or TAWS (data latency) have on the accuracy of detection range predictions. Then the improvement in allocation of search assets during adverse weather conditions, which resulted from the use of NPOESS-resolution data, was considered. Finally, new output quantities from TAWS that will be required as input to combat attrition models were identified for future implementation.</p>					
15. SUBJECT TERMS DMSP NPOESS tactical decision aids weather					
16. SECURITY CLASSIFICATION OF:			17. LIMITATION OF ABSTRACT U	18. NUMBER OF PAGES 62	19a. NAME OF RESPONSIBLE PERSON Sean O'Brien
a. REPORT U	b. ABSTRACT U	c. THIS PAGE U			19b. TELEPHONE NUMBER (Include area code) (505) 678-1570